Precambrian Research 395 (2023) 107129

Contents lists available at ScienceDirect

Precambrian Research

journal homepage: www.elsevier.com/locate/precamres

Himalayan magnesite records abrupt cyanobacterial growth that plausibly triggered the Neoproterozoic Oxygenation Event

Prakash Chandra Arya [a], Claude Nambaje [a,1], S. Kiran [b], M. Satish-Kumar [b,*], K. Sajeev [a,*]

[a] Centre for Earth Sciences, Indian Institute of Science, Bengaluru 560 012, India
[b] Department of Geology, Niigata University, Niigata 950-2181, Japan

ARTICLE INFO

Keywords:
Neoproterozoic Snowball Earth
Himalayan sparry magnesite
Cyanobacteria
Earth's oxygenation
Neoproterozoic seawater/oceanwater droplets

ABSTRACT

The widespread glaciation (~750–580 Ma) of the late Neoproterozoic Snowball Earth and the subsequent (~630–551 Ma) oxygenation of the oceans and atmosphere were critical factors in microbial evolution and the following ~540–520 Ma explosion of complex life forms in the Cambrian. However, the underlying mechanisms that link these processes are still unclear due to poorly preserved fossil records and the tectonic destruction of the paleo-oceans, limiting our understanding of the Neoproterozoic Earth, a key time when unicellular life evolved into complex forms. Droplets of Neoproterozoic oceanwater and freshwater trapped in Himalayan crystalline magnesite ($MgCO_3$) show that sedimentary basins were deprived of calcium for an extended period during the Snowball Earth glaciation, probably due to low riverine input of the dissolved products of weathering. Protracted precipitation of calcite-dolomite in a closed basin, now exposed in Kumaun Himalayas, Uttarakhand (India), decreased the Ca/Mg ratio in the seawater. This fall in the Ca/Mg ratio—initiated magnesite precipitation and increased the basin's oligotrophy (nutrition deficiency). The slow-growing photosynthetic cyanobacterial stromatolites could thrive in such oligotrophic conditions. The same is reflected in the field, i.e., the appearance of stromatolites towards the end of dolomite formation and their population expansion in the overlying magnesite beds. Continued magnesite precipitation in a closed basin, driven by positive feedback, resulted in high photosynthetic oxygen production, conceivably triggering the Neoproterozoic Oxygenation Event and stimulating Cambrian Explosion.

1. Introduction

Several environmental and atmospheric changes during the Proterozoic Eon were vital factors in shaping the evolution of life, such as—the ~2400 Ma Paleoproterozoic Snowball Earth (Kirschvink et al., 2000), the ~2300 Ma Great Oxygenation Event (Luo et al., 2016), the ~750–580 Ma periods (Fairchild & Kennedy, 2007) of Neoproterozoic Snowball Earth (Pierrehumbert et al., 2011), and the ~630–551 Ma Neoproterozoic Oxygenation Event (Sahoo et al., 2012). Even though oxygen is the third most abundant element in the universe (Anders & Grevesse, 1989) and the most abundant element in Earth's crust, the Earth's environment remained reducing for a prolonged time (Canfield, 2005). After the Great Oxygenation Event, once again, the oxygen concentration started rising during the Neoproterozoic-Phanerozoic transition, and for the first time, the oxygen concentration reached the present atmospheric levels (Berner, 2006; Berner et al., 2003; Canfield, 2005; Nursall, 1959). This transition is considered the most crucial time for rapid biological evolution because oxygen was available for simple life forms to drive the metabolism required for complex forms (Catling et al., 2005). After the Neoproterozoic Oxygenation Event, complex life evolved rapidly—the ~540–520 Ma so-called Cambrian Explosion (Canfield et al., 2007). It has been observed that the Snowball Earth Events are followed by stepwise oxygenation of the Earth (Kirschvink et al., 2000; Luo et al., 2016). With each oxygenation, more complex life forms developed (Alcott et al., 2019). The first eukaryotes evolved during or after the Great Oxygenation Event. Similarly, the major eukaryote diversification leading to the Cambrian Explosion coincided with the Neoproterozoic Oxygenation Event (Alcott et al., 2019), a key time when unicellular life evolved towards the complex forms that we see today (Pierrehumbert et al., 2011).

The Snowball Earth Events, Earth's oxygenation, and biological evolution are closely related (Luo et al., 2016), but the relationship is

* Corresponding authors.
E-mail addresses: satish@geo.sc.niigata-u.ac.jp (M. Satish-Kumar), sajeev@iisc.ac.in (K. Sajeev).
[1] Current address: Trinity Metals Ltd, Rwanda.

https://doi.org/10.1016/j.precamres.2023.107129
Received 4 June 2022; Received in revised form 31 January 2023; Accepted 30 June 2023
Available online 17 July 2023

poorly understood (Alcott et al., 2019; Kirschvink et al., 2000; Sahoo et al., 2012), limiting our understanding of the paleoenvironment and the mechanisms behind the Cambrian Explosion. Knowledge of biological radiation requires a thorough understanding of the above processes, along with the geochemical and environmental aspects of the Neoproterozoic (Halevy & Bachan, 2017; Sahoo et al., 2012). Unfortunately, most of the information needed is missing or poorly preserved—paleo-oceans have been tectonically destroyed, and the atmosphere's composition has changed considerably since that time.

There are no rock-forming minerals that undergo deposition from the atmosphere to preserve the paleo-atmospheric composition. Minerals precipitated from seawater, however, have the potential to preserve evidence of their paleo-oceans. Magmatic, metamorphic, and hydrothermal fluids are commonly trapped in rock-forming minerals (Bodnar, 2006), but inclusions of paleo-ocean are rarely known because carbonates, the most common marine precipitate, are mostly too fine-grained (Kazmierczak & Altermann, 2002), readily recrystallized, and chemically altered (Satish-Kumar et al., 2021b). Himalayan magnesite is a rare exception. By integrating geochemical, isotopic, fluid inclusion, and spectroscopic studies of such magnesite, we have shown that long-lived glacial events produce significant changes in the biota and the chemical composition of the oceans and atmosphere, resulting in the release of large amounts of oxygen, a likely a first-order trigger of the Neoproterozoic Oxygenation Event and stimulating Cambrian Explosion.

1.1. Geological setting of the study area

The study area lies in the central sector of the Himalayas, i.e., the Lesser Himalayas of the Kumaun (Fig. 1**A**). This region falls in the Uttarakhand state of India. The Lesser Himalayas of the Kumaun represents one of the recognized Precambrian basins in India (Singh, 2019; Singh et al., 2009) and is subdivided into Inner Lesser Himalayas and Outer Lesser Himalayas (Etienne et al., 2011; Raha & Sastry, 1982; Schelling, 1992; Tewari & Seckbach, 2011). The Deoban Formation in the Kumaun is a thick succession of marine carbonates. It is a part of the Inner Lesser Himalayas and is present throughout the Himalayan arc. These carbonates beds extend from northwest of Pakistan to the east of India, i.e., Arunachal Pradesh, and are known by various names in different regions of the Himalayas, such as Jammu Limestone in Riasi region of Jammu and Kashmir (India), Shali in Himachal Pradesh

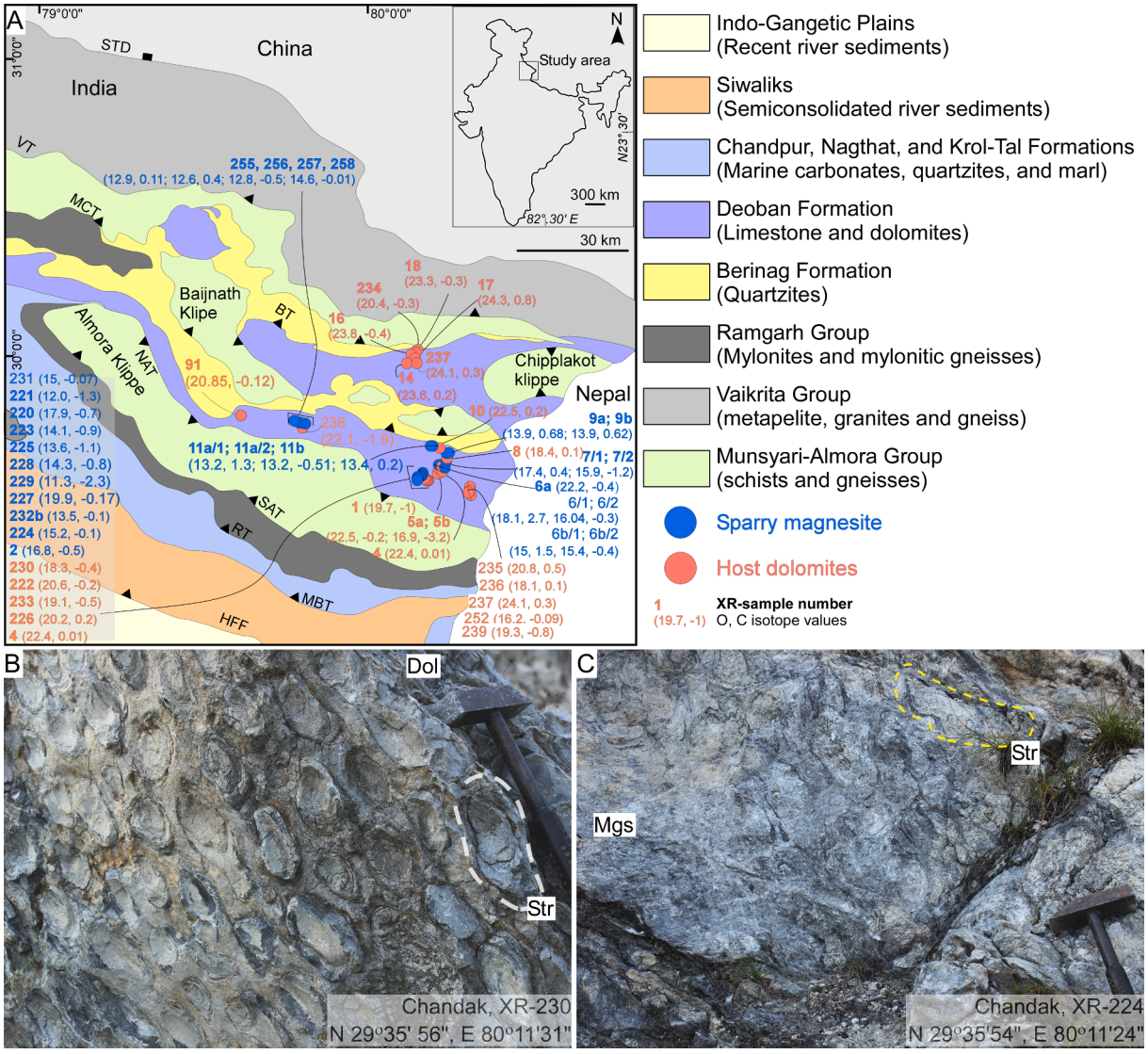

Fig. 1. Neoproterozoic carbonates of the Kumaun Himalayas. **A)** Study area marked (black box) in the India's map along with the sample location's C–O isotopic composition. **B)** Stromatolites (Str) in dolomite (Dol). **C)** Relatively larger stromatolites in sparry magnesite (Mgs). The map is modified after Valdiya (1980). **Acronym:** HFF—Himalayan Frontal Fault, MBT—Main Boundary Thrust, RT—Ramgarh Thrust, SAT—South Almora Thrust, NAT—North Almora Thrust, BT—Berinag Thrust, MCT—Main Central Thrust, VT—Vaikrita Thrust, STD—South Tibetan Detachment.

(India), Deoban in Uttarakhand (India), Dhading in Nepal, Buxa in Darjeeling–Sikkim–Bhutan sector, Dedza in western Arunachal Pradesh (India). In Pakistan, it is known as Sirban or Shahkot Formation (Tewari, 2007; Tewari & Sial, 2007; Valdiya, 2015).

The lithological column, modified after Tewari and Sial (2007), describes the stratigraphy of the Kumaun Lesser Himalayas **(**Fig. 2**)**. Berinag Formation is the oldest (~ 1870 Ma) sedimentary record in Kumaun (Mukherjee et al., 2019), above which lies the Chakrata and Rautgara Formaitons respectively. Stratigraphically, the Deoban Formation lies above the quartzites of the Rautgara Formation, having a maximum deposition age (detrital zircons) of ~754 ± 16 Ma (Negi et al., 2022), over which lies Chandpur Formation (phyllites, shales, and slates). The Chandpur Formation is overlain by the Nagthat Formation (quartzites), having a maximum deposition age (detrital zircons) of ~743 ± 5 Ma (Negi et al., 2022). The Nagthat Quartzites are overlain by Blaini Formation (maximum deposition detrital zircon age ~678 ± 10 Ma) (Hofmann et al., 2011), the Blaini Formation is considered as cap carbonates of Kumaun, over which lies Krol (Terminal Proterozoic) and Tal Formation (Early Cambrian) (Tewari & Sial, 2007).

A Vendian ~650 to 543 Ma microfossil (protoconodonts) age is reported from the Deoban Formation (Azmi & Paul, 2004). Moreover, the Vendian sponge spicules and organic-walled microfossils were found in the studied magnesite-bearing Chandak member of the Deoban Formation (Tiwari et al., 2000; Tiwari & Pant, 2009), suggesting the Deoban carbonates (magnesite and dolomite) were formed during the Vendian time. These carbonates were plausibly precipitated from the Proto-Tethys Ocean, which was known to exist during that time (Zhang et al., 2018).

2. Materials and methods

2.1. Data collection and processing

2.1.1. Field

In the field, sedimentary structures, fossil assemblage, and geolocation were carefully recorded while sampling. The geological map (Valdiya, 1980) of the Kumaun Himalayas was georeferenced using ArcGIS 2010 (Bajaj & Arya, 2021; Herbei et al., 2010) and the field information (geolocation, rock types) was added to it. To enhance image clarity, labelling on the map was done using Canvas X-GIS 2020.

2.1.2. Petrology

Thin sections of the carbonates (dolomite and magnesite) were prepared using a standard protocol (Reed & Mergner, 1953) and were mirror polished. Olympus BX-51 at the Centre for Earth Sciences (CEaS), Indian Institute of Science (IISc), Bengaluru, India, was employed for petrological observations (e.g., texture and assemblage) and collecting photomicrographs. To enhance image clarity, labelling on the photomicrographs was done using Canvas X-GIS 2020.

2.1.3. Major, trace, and rare Earth element (REE) chemistry

JEOL JXA 8230 EPMA at Advanced Facility for Microscopy and Microanalysis (AFMM), IISc Bengaluru, was used to analyze mineral oxides using analytical conditions of 15 kV acceleration voltage, 12nA probe current, and 3 μm electron beam size. Calibration was done on natural minerals, and the generated data (**Supplementary Table S1**) was processed using the oxide-ZAF correction. Whole-rock powder of the dolomite and magnesite was analyzed for trace and REE concentrations, and BHVO-2, W-2a, and JB-2 standards were used. Standard protocols were followed for sample preparation (Satish-Kumar et al., 2021b). All analyses were carried out using a standard protocol with an Agilent 7500 ICP-MS at Niigata University, Japan (Neo et al., 2009). The trace and PAAS normalized Rare Earth Element (REE) data are given in **Supplementary Table S2**.

2.1.4. Stable isotopic composition

Small (~4 cm × 2 cm × 1 cm) chips of magnesite and dolomite were grinded up to 1000 grit SiC powder. The subvolume from these chips was extracted using a tapering head dentist drill of a 1 mm diameter. Among magnesite (n = 23) samples, one individual measurement (C–O) was carried out from nineteen samples, whereas two measurements were carried out from each of the remaining four samples (XR-6, XR-6b, XR7, XR-11a). For dolomites (n = 23), one measurement was done for each sample. For consistency, all oxygen isotopic data (measured in this study or taken from published articles) was converted to the V-SMOW scale (Joachimski et al., 2004). Thermo Fischer MAT-253 mass spectrometer housed at Niigata University, Japan was used for isotopic analysis. The details of the analytical methods are given in a published article (Satish-Kumar et al., 2021a).

Age and C–O isotopic data of sparry magnesites and host carbonates were collected from published literature from all over the world, i.e., Australia (Aharon, 1988), Spain (Herrero et al., 2011; Kilias et al., 2006; Kralik & Hoefs, 1978), Austria (Azim Zadeh et al., 2015; Henjes-Kunst et al., 2014; Spötl & Burns, 1994), Italy (Lugli, 2001), Russia (Melezhik et al., 2001), Quebec (Peck & Eppich, 2019), China (Misch et al., 2018; Tang et al., 2013), Brazil (Parente et al., 2004), Mexico (Garber et al., 1990), and India (Joshi & Pant, 2017; Sharma, 2006). When C–O isotope data table was unavailable, their values were approximated from the published plots.

Apart from sparry magnesite and host carbonates from different parts of the world, the C–O isotopic data (Knauth & Kennedy, 2009) of the marine carbonates of the Archean-Palaeoproterozoic, Mesoproterozoic, Neoproterozoic, and Phanerozoic time is also used for comparison purpose and are named as Reference Carbonates **(Supplementary Table S3)**. For accurate plotting of C–O isotopes, only those data were used where both carbon and oxygen values were available. For ease of visualization, plotting, and broader comparison, we have taken the average age of the reference carbonates (i.e., Knauth and Kennedy's dataset) and published age of the other carbonates to generate Fig. 6. The isotopic data were combined with field and textural data **(Supplementary Table S4)** to understand their relation. All isotopic data analyses were performed in R (version 3.6.3). To enhance clarity, labelling on the image was performed in Canvas X-GIS 2020.

2.1.5. Fluid inclusion and microthermometry

Nearly 100–120 μm thick doubly mirror-polished wafers of the magnesite and dolomite were prepared (McNeil & Morris, 1992) at the CEaS, IISc Bengaluru, India. The wafers were temporarily attached to the glass slide using honeybee wax. The final wafer were washed in hot (~75 °C) toluene for half an hour. After the toluene bath, the wafers were carefully wiped with ethanol, rinsed with deionized water, dried, and kept inside polypropylene zip lock covers until analysis. All fluid inclusions were identified under Olympus BX-51 (mentioned above) at 20X or 50X magnification. The microthermometric analysis was done using a Linkam Fluid Inclusion heating and cooling stage (TS 600) attached to Olympus BX-41 available at CEaS, IISc Bengaluru (India). Microthermometry was conducted as per the available methodology (Walderhaug, 1994). The 'FLUIDS' package was used to model bulk fluid properties such as density (Zhang & Frantz, 1987) and salinity (Bodnar, 1993). The fluid inclusions data **(Supplementary Table S5)** analysis was performed in R (version 3.6.3).

2.1.6. Infrared (IR) and Raman spectroscopy

Regions containing abundant fluid inclusions in the magnesite wafers that are free from cracks and fractures, were selected to collect the IR spectra. The selected wafers (~3 × 3 mm size) were kept in 2 ml Eppendorf tubes until analysis. We collected 24 IR spectra from 23 individual samples, two of them were collected from one sample (XR-6) to see the variation of spectra from a fluid-rich region to a fluid-deficient region. Among the water samples, one IR spectra was taken from Kaveri River water (RW), one from filtered tap water (TW), two from

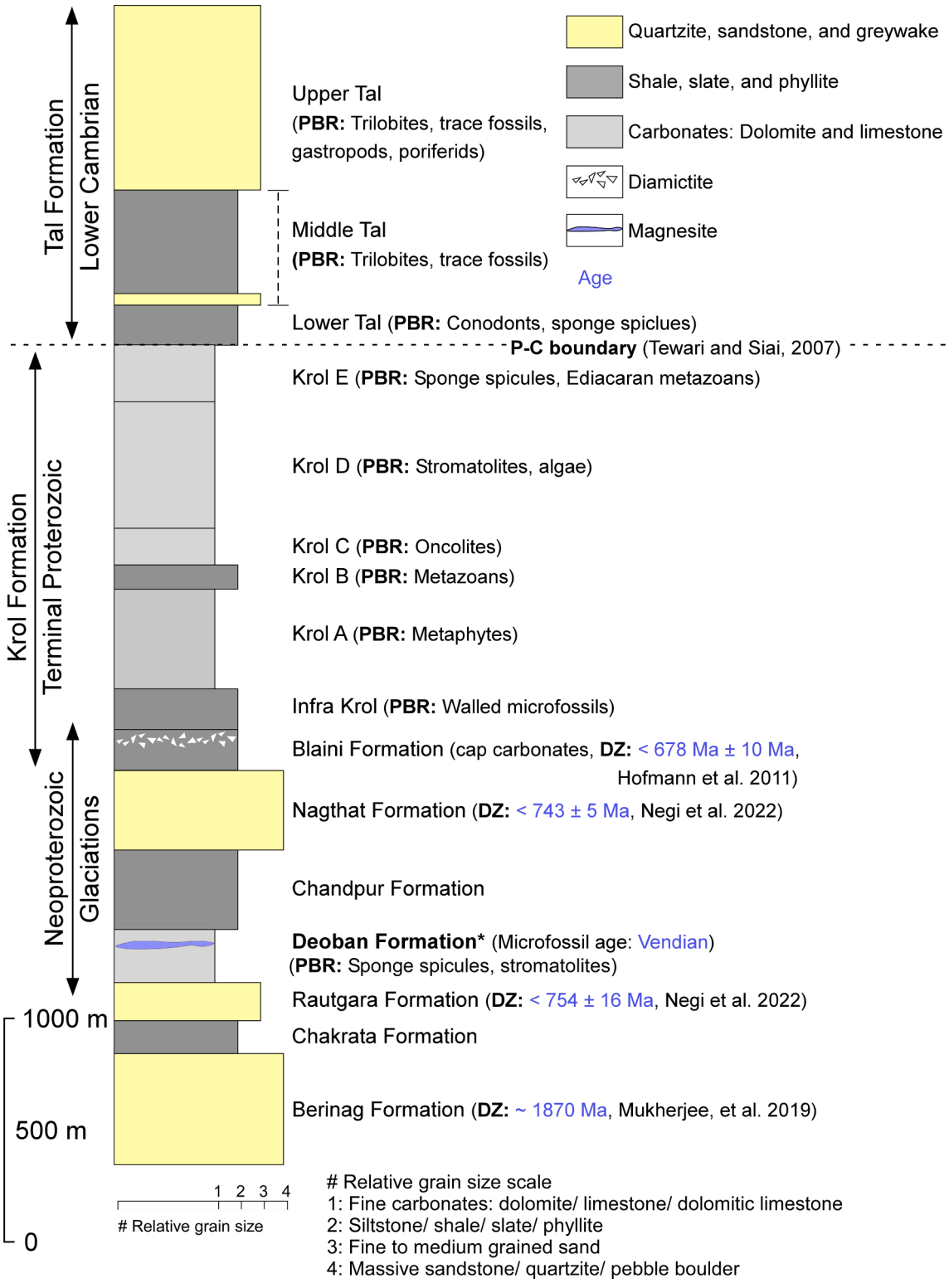

Fig. 2. Lithostratigraphic column of the Kumaun Lesser Himalayas. The ages are highlighted in blue. The formations are marked with their detrital zircon (DZ) age and their palaeobiological remains (PBR). The lithostratigraphic column diagram and palaeobiological remains are taken from Tewari and Sial (2007).

oceanwater (OW1 and OW2), and two from deionized water samples DW1 (taken from CEaS, IISc) and DW2 (taken from Molecular Biophysics Unit (MBU), IISc). All IR spectra were collected in ATR (Attenuated Total Reflectance) mode of the Fourier transform infrared (FTIR) spectroscope available at the Optical Characterisation Laboratory of Centre for Nano Sciences (CeNSE), IISc Bengaluru, India. Nearly the entire spectral range was scanned, i.e., 650 to 4000 cm^{-1}. During the analysis, thirty-two accumulations were taken, and the gauge value was maintained between 19 and 22 to avoid damaging of the sample or the sensor. The Raman spectra (between 50 and 4000 cm^{-1}) were collected

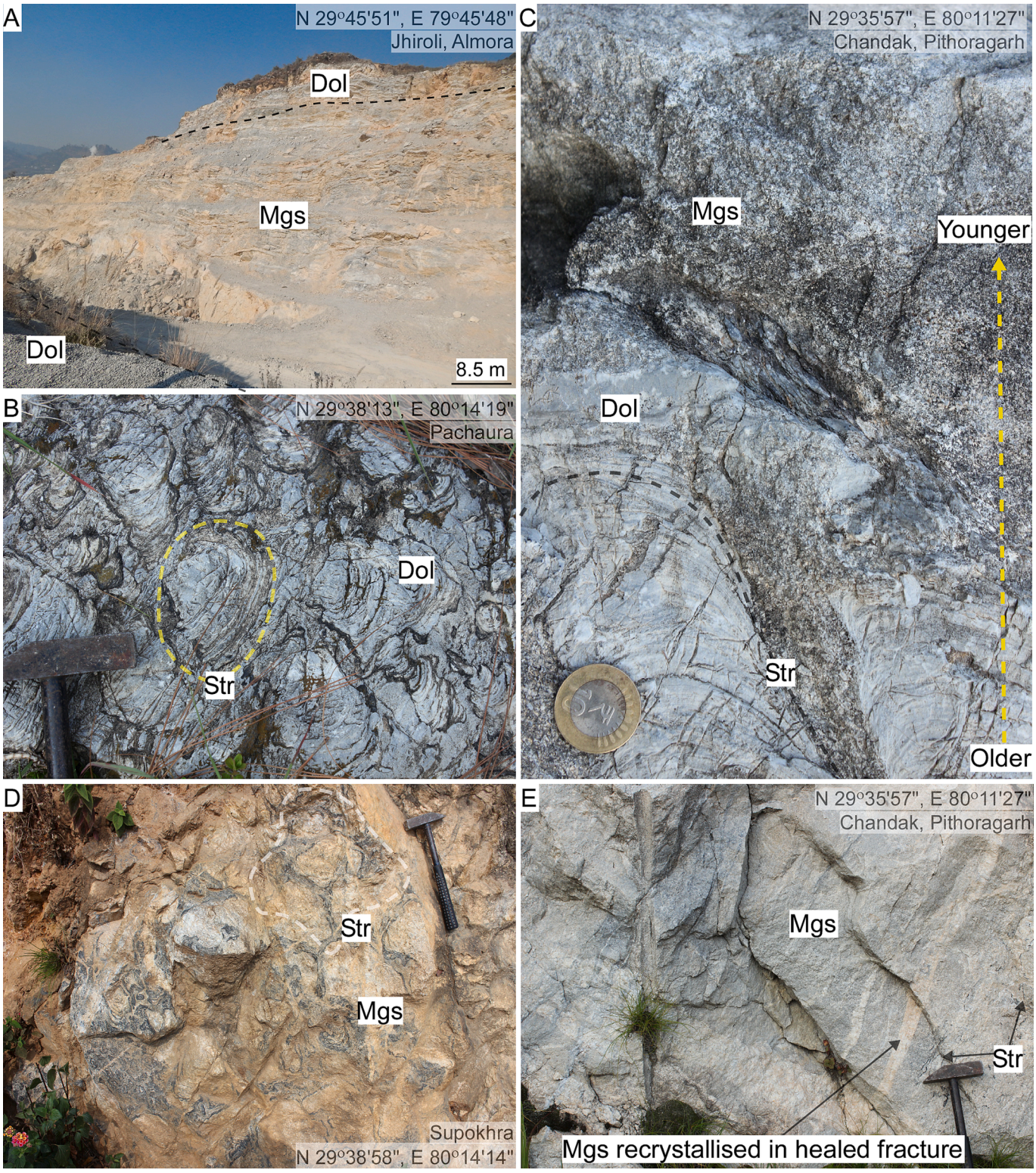

Fig. 3. Field relationships and evidence. A) Thick magnesite beds along with host dolomites. **B)** Stromatolite-bearing host dolomites. **C)** Gradation of carbonate sequence from dolomite (older) to magnesite (younger), identified from the shape of the stromatolites, i.e., convex upwards. **D)** Relative to dolomite, larger-size stromatolites in the sparry magnesite **E)** Recrystallized coarse-grained magnesite vein within equigranular magnesite. **Acronym:** Dol—Dolomite, Mgs—Magnesite, Str—Stromatolite.

from the fluid inclusions and the surrounding magnesite wafer using LabRAM HR available at CeNSE, IISc Bengaluru, India. Raman spectra were collected using 532 nm InGaAs laser, 1800 g/mm grating, 50X objective, 100% filter. The collected spectral data, i.e., Infrared spectra **(Supplementary Table S6)** and Raman spectra **(Supplementary Table S7),** were normalized and plotted in MATLAB (version R2020b). The Raman peaks were verified through published articles, CrystalSleuth and the RUFF database.

2.1.7. Statistical analysis

The field, isotopic, and textural data were combined for statistical analysis **(Supplementary Table S4)**. A two-tailed paired *t* test was performed in Microsoft Excel 365 to test null hypotheses H1, H2, H3, H4, H5, and H6. H1-Oxygen isotopic composition of dolomites and magnesite are similar. H2-Oxygen isotopic composition of the carbonates (dolomite and magnesite) does not vary due to presence or absence of stromatolites. H3-Oxygen isotopic composition does not vary due to grain size or crystallinity. H4-Carbon isotopic composition of dolomites and magnesite are similar. H5-Carbon isotopic composition of the carbonates (dolomite and magnesite) does not vary due to presence or absence of stromatolites. H6-Carbon isotopic composition does not vary due to grain size or crystallinity. All statistical analysis was performed in R version (3.6.3). *P* values below 0.05 were considered statistically significant.

3. Results

3.1. Field evidence

In Kumaun, the Deoban Formation lies between the North Almora Thrust (NAT) and Berinag Thrust (BT) **(**Fig. 1**A).** It consists of limestone, dolomitic limestone, and dolomites. The stratabound magnesite beds in the Deoban Formation are nicely exposed towards the eastern side of the Kumaun **(**Fig. 1**A).** In the field, the stromatolites were observed in the dolomites and magnesites **(**Fig. 1**B and C).** A thick dolomite sequence of the Deoban Formation transitions upward to pure and homogeneously distributed magnesite beds **(**Fig. 3**, A–E).** Sedimentary features were dominantly seen in the field, such as 1) Occurrence of dolomites and magnesites as beds, 2) Presence of stromatolites in both, alongwith the absence of any traces of hydrothermal or mafic magmatism **(**Fig. 3,

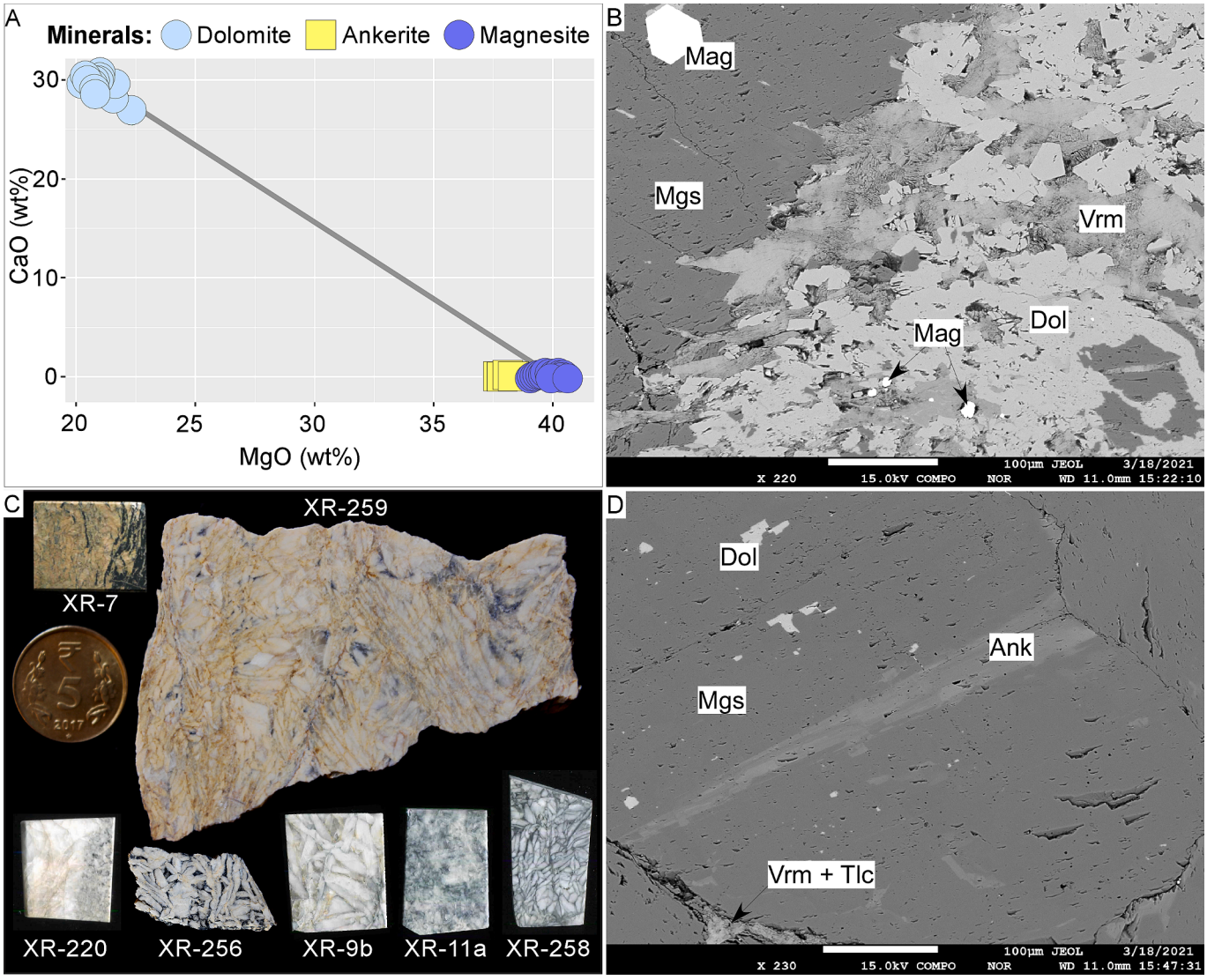

Fig. 4. Microtextures, mineral assemblage, and mineral chemistry of the carbonates of the Kumaun Himalayas. A) CaO Vs MgO of magnesite, dolomite, and ankerite in sparry magnesite. **B)** Backscattered electron image showing associated clay minerals with dolomite. **C)** Needle-shaped texture of the sparry magnesites in shades of yellow, white, and grey. **D)** Backscattered electron image of the sparry magnesite crystals with small dolomite inclusions. **Acronym:** Dol Dolomite, Mgs—Magnesite, Ank—Ankerite, Vrm—Vermiculite, Tlc—Talc, Mag—Magnetite.

A–E). The stromatolites first appeared in the dolomites lying immediately below younger magnesite beds **(**Fig. 3**C)**, increasing in density and size contrast in the latter **(**Fig. 1**B and C) and (**Fig. 3**B and D)**. The increase in size and density of microbialites in magnesite relative to the dolomite was observed in all visited locations (i.e., Jhiroli, Chandak, and Supokhra). Further, the magnesite horizons appear chemically pristine and are homogeneously distributed, and no associated detrital sediments were encountered during the field survey **(**Fig. 1**C) and (**Fig. 3**, C–E)**. Coarse-grained magnesite veins are found within the equigranular matrix of yellow-white magnesite beds **(**Fig. 3**E)**.

3.2. Mineral chemistry and REE distribution of the Deoban carbonates

Mineral Chemistry: The microprobe analysis revealed the MgO and CaO concentration of the dolomite range from ~21–22 % and ~27–31 %, respectively **(**Fig. 4**A) (Supplementary** Table S1**)**. These dolomites are commonly associated with clay minerals **(**Fig. 4**B)** with minor microcrystalline quartz **(Supplementary** Table S1**)**. The magnesite, in contrast, are coarsely crystalline **(**Fig. 4**C)** and chemically pure **(**Fig. 4**D),** with MgO concentration varying between ~39–41 %, <3 % FeO, and other oxide impurities are < 1 % **(Supplementary** Table S1**)**. Minor amount of dolomite, ankerite, vermiculite, and talc occur as inclusions or occupy interstitial spaces **(**Fig. 4**D)**.

Rare Earth Element distribution: The REE pattern of the dolomites and magnesites shows a flat profile **(**Fig. 5**)**. However, two magnesite samples from recrystallized veins had a slight positive Eu anomaly **(**Fig. 5**)**. The **Supplementary** Table S2 depicts the superchondritic Y/Ho ratio of the host dolomites (average ~52.93) and sparry magnesites (average ~44.67), the average $[Ce/Ce^*]_N$ of the dolomites and magnesites are ~0.89 and ~0.95, respectively, the average $[Gd/Gd^*]_N$ of the dolomite and magnesite are ~1.43 and ~1.23, respectively, the average Er/Nd of the host dolomites and magnesites are ~1.42 and ~4.02, respectively. Low concentrations of redox-sensitive elements were found in dolomites and sparry magnesite, e.g., authigenic U of dolomites (average ~0.05) and magnesites (average ~0.16), U of dolomites (average ~0.07) and magnesites (average ~0.17), V of dolomites (average ~1.36) and magnesites (average ~2.33), Co of dolomites (average ~1.10) and magnesites (average ~0.73), Cr of dolomites (average ~2.11) and magnesites (average ~0.57).

3.3. Carbon and oxygen isotopic signatures of Deoban carbonates

The carbon and oxygen isotopic compositions of the worldwide sparry magnesite closely match the isotopic composition of the marine carbonates (Knauth & Kennedy, 2009) of the same age **(**Fig. 6**A and B) and (**Fig. 7**) (Supplementary** Table S3**)**. The carbon isotopic compositions ($\delta^{13}C$, VPDB) of the Kumaun magnesite and dolomite range between (−2.3 to +2.7 ‰) and (−3.2 to +0.8 ‰), respectively **(**Fig. 6**B) (Supplementary** Table S3**)**. The $\delta^{13}C$ does not vary between magnesite and their host dolomites, whether the rock is coarsely crystalline or fine-grained, and whether stromatolites are present or not (two-tailed *t* test, $P > .05$) **(**Fig. 6**B and** Fig. 8**A) (Supplementary** Table S4**)**. There is a large difference, however, between the oxygen isotopic composition ($\delta^{18}O$, VSMOW) of the magnesites (average ~15 ‰) and host dolomites (average ~21 ‰). The $\delta^{18}O$ value depends on whether the rock is coarsely crystalline or fine-grained, and whether stromatolites are present or not (two-tailed *t* test, $P < .001$) **(**Fig. 6**B and** Fig. 8**B)**. Coarsely-crystalline or stromatolite-bearing dolomites have lower $\delta^{18}O$ values (average ~19 ‰) relative to the fine-grained non stromatolite-bearing dolomites (average ~22 ‰) **(Supplementary** Table S4**)**. The coarsely-crystalline and stromatolite-bearing sparry magnesites have significantly lower $\delta^{18}O$ values (average ~15 ‰) than stromatolite-bearing host dolomites (average ~19 ‰) **(Supplementary** Table S4**)**.

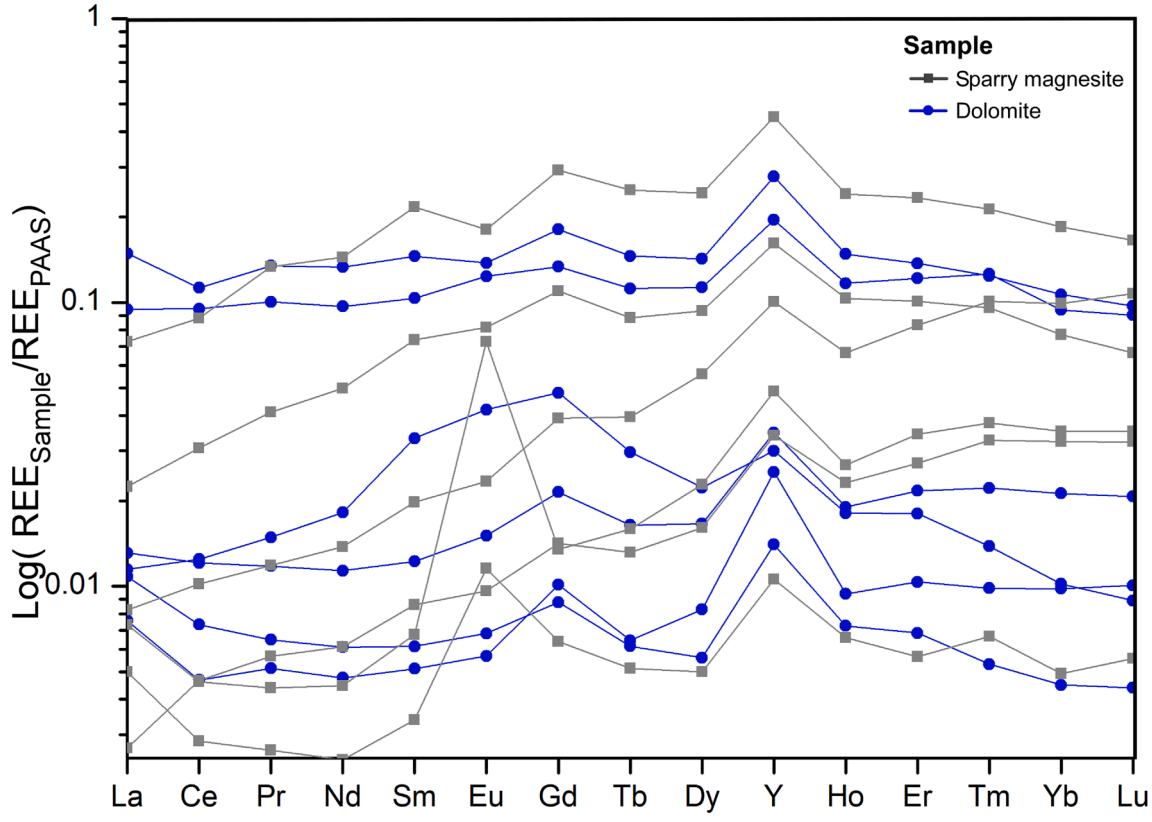

Fig. 5. PAAS normalized REE distribution in the sparry magnesite and the host dolomite of the Kumaun Himalayas.

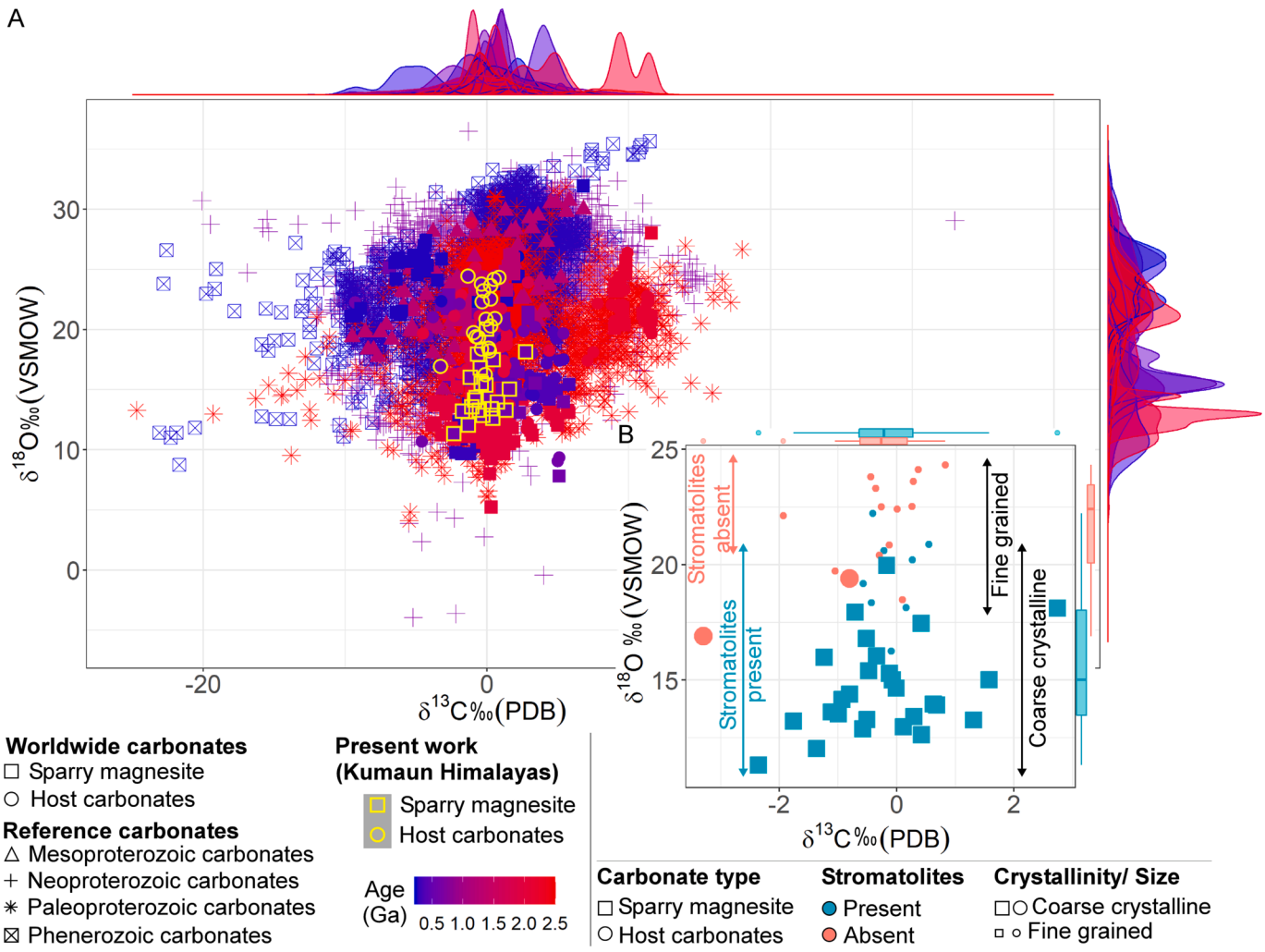

Fig. 6. C–O isotopic composition of the Deoban carbonates. **A)** C–O isotopic and age comparison of Deoban Formation with worldwide sparry magnesite, their host, and the reference carbonates. Color of the points and density distribution corresponds to the age (in Ga) given in the scale bar. **B)** C–O isotope variation between stromatolite bearing/ non-bearing, coarse/ fine-grained magnesite and dolomites of Kumaun.

3.4. Fluid inclusions and modelled salt complex in Deoban sparry magnesites

Among magnesite and dolomite, the fluid inclusions were found in the magnesite and were absent in dolomite wafers. Nine magnesite samples contained sufficiently large aqueous fluid inclusions that are suitable for fluid inclusion studies. The fluid inclusions in the remaining magnesite samples were too small to analyze. The sparry magnesite contains primary (P) and pseudosecondary (PS) bi-phase aqueous fluid inclusions. The size of the fluid inclusions is up to 15 μm **(**Fig. 9**A and B) (Supplementary** Table S5**)**. Based on salinity and final ice melting temperatures, three types of fluid inclusions (F1, F2, and F3) were identified **(**Fig. 9**C and D)**. Primary F1 fluids are very dense (1.19–1.15 g/cc) and saline (25.02–20.52 eq. NaCl), with a final ice melting temperature (T_f) between −24.1 and −17.4 °C. Primary and pseudosecondary F2 fluids are moderately dense (1.13–1.08 g/cc) and saline (17.87–10.86 eq. NaCl), with a T_f between −14.1 and −7.3 °C. Pseudosecondary F3 fluids are least dense (1.05–1 g/cc) and have extremely low salinity (7.73–0.18 eq. NaCl), with a T_f between −4.9 and −0.1 °C **(Supplementary** Table S5**)**. Microthermometry and fluid modelling suggest the presence of $MgCl_2$-$CaCl_2$-NaCl-KCl salt complex in the fluid inclusions.

3.5. Infrared and Raman spectra of fluid-bearing sparry magnesite

Wafers of fluid-bearing sparry magnesite free from cracks and fractures were analyzed using ATR-FTIR **(Supplementary** Table S6**)**. The first intense band is observed at ~740–745 cm^{-1} **(**Fig. 10**A)**. The second and third intense bands are observed at ~850–852 cm^{-1} and ~860–890 cm^{-1}, respectively **(**Fig. 10**A)**. A weak broad band is observed at ~1300–1450 cm^{-1} **(**Fig. 10**A and B)**. Strong absorption is observed at ~2540 cm^{-1}, ~2850 cm^{-1}, and ~2920 cm^{-1}. The magnesite wafers also show absorption corresponding to ~1634, ~2000–2200, and ~3000–3500 cm^{-1} **(**Fig. 10**A and C)**. The IR absorption at ~1050–1170 cm^{-1} (centred ~1100 cm^{-1}) is found in sparry magnesites. Raman data **(Supplementary** Table S7**)** shows sharp Raman peaks at ~212, ~328, and ~1094 cm^{-1}, while smaller peaks were present at ~1446 and ~1763 cm^{-1} **(**Fig. 11**, A–C)**.

4. Discussion and implications

4.1. Neoproterozoic carbonates and stromatolites of the Kumaun Himalayas

The Vendian (~650–543 Ma) Deoban Formation in the Kumaun Himalayas preserves the carbonate succession of the Neoproterozoic time. The stromatolite-bearing (Valdiya, 1968) dolomites and

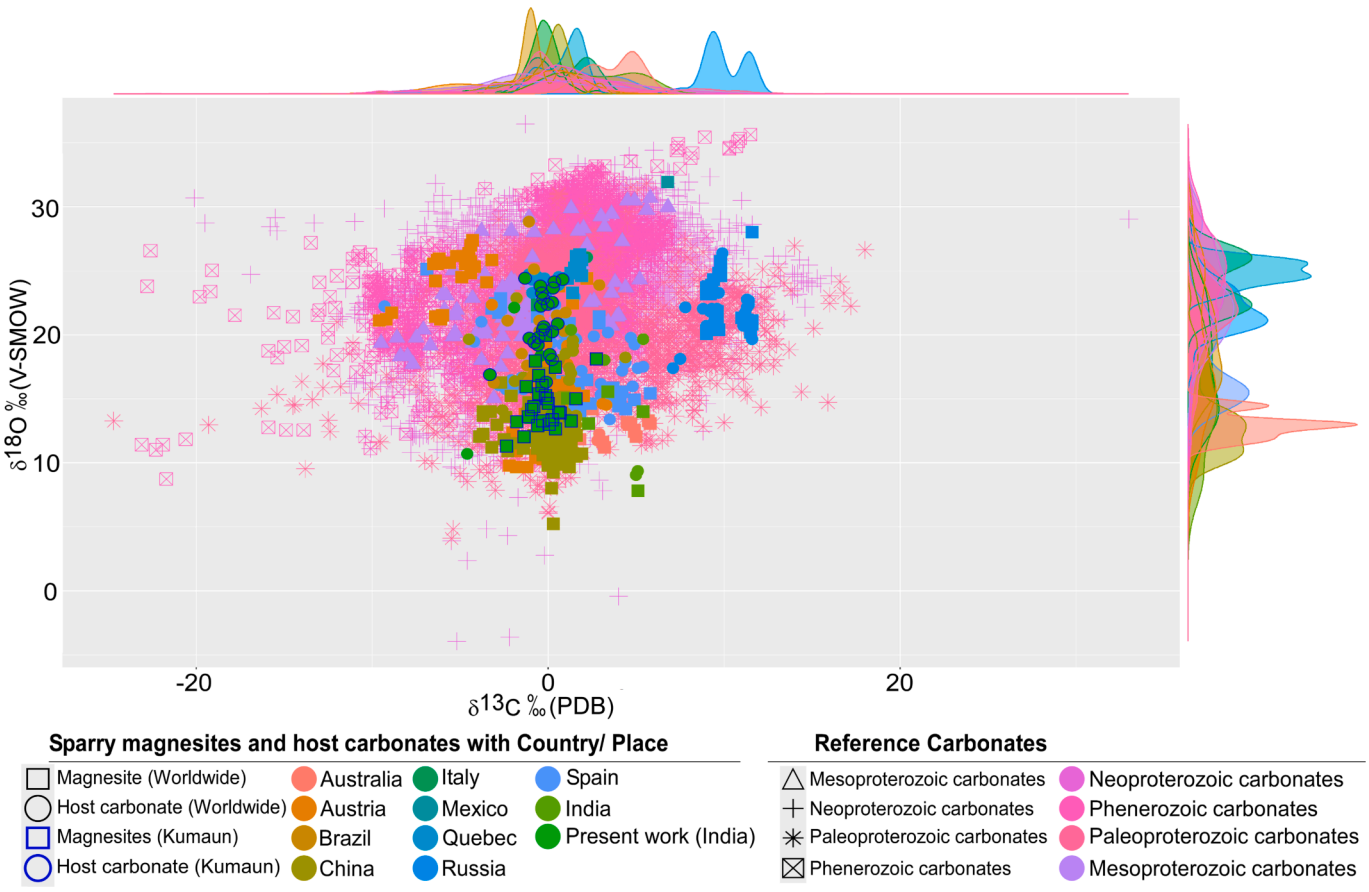

Fig. 7. C–O isotopic comparision of the worldwide sparry magnesites with marine carbonates. Carbon and oxygen isotopic composition of sparry magnesite from the Kumaun Himalayas compared with sparry magnesite and marine carbonates (Knauth & Kennedy, 2009) from different parts of the world. The compiled global isotopic data (sparry magnesite and host dolomites) are from Australia (Aharon, 1988), Spain (Kralik & Hoefs, 1978; Kilias et al., 2006; Herrero et al., 2011), Austria (Spötl & Burns, 1994; Henjes-Kunst et al., 2014; Azim Zadeh, Ebner & Jiang, 2015), Italy (Lugli, 2001), Russia (Melezhik et al., 2001), Quebec (Peck & Eppich, 2019), China (Tang et al., 2013; Misch et al., 2018), Brazil (Parente et al., 2004), Mexico (Garber et al., 1990), and India (Sharma, 2006; Joshi & Pant, 2017). Different symbols represent rock types and reference carbonates. The color corresponds to different countries and reference carbonates, as the legend displays. The highlighted samples in blue squares and circles represent the sparry magnesite and host dolomite of the Kumaun Himalayas, respectively.

magnesites were deposited during the Cryogenian period, dominated by Snowball Earth glaciation (Tiwari and Pant, 2009), plausibly from the Proto-Tethys Ocean. All field evidence, such as bedding in dolomites, stratified magnesite horizons, stromatolites in magnesite and dolomite, absence of dyke, and no traces of hydrothermal and mafic intrusions (Fig. 3**A–E)**, point towards a sedimentary origin of the magnesites and the dolomites (Schulz & Vavtar, 1977)**.** The chemically pure and homogeneously distributed stromatolite-bearing magnesite horizons traceable for several hundred kilometres along the strike also argue against a possible hydrothermal setting; the homogeneity of sparry magnesite rather represents the homogeneously distributed sediments in the Deoban basin (Valdiya, 1968). The continued growth of the stromatolites during the upward transition of the dolomite to magnesite suggests both are a part of the same carbonate sequence and were precipitated within the photic zone of a shallow marine environment (Banerjee et al., 1986). A sudden increase in the population density and size of the microbialites in the magnesite relative to the underlying dolomites reflects the sensitivity of the microbial mats towards change in the chemistry of the basin, i.e., calcium deficiency during magnesite precipitation (Fig. 1**C and** Fig. 3, **D–E)**. The coarse-grained white magnesite veins within equigranular yellow-white magnesite (Fig. 3**E)** possibly represent healed fractures due to local deformation (Valdiya, 1968). Our comprehensive field study clearly shows the Deoban basin underwent extreme physicochemical changes in the Neoproterozoic that led to a sudden biological or ecological response of the cyanobacterial stromatolites during magnesite formation. This information is vital for understanding the chemical and biological evolution of the Precambrian basins (especially Neoproterozoic) as it plays a critical role in understanding the Precambrian ecological niches, life forms and their response to the distribution of resources and competitors.

4.2. *Carbonate chemistry points towards an oxygenic environment*

The dolomites are consistent in composition (~21–22 % MgO, ~ 27–31 % CaO) but are commonly associated with negligible amounts of clay minerals and microcrystalline quartz washed in by the rivers feeding the basin (Fig. 4**A and B) (Supplementary Table S1)**. The continental-derived impurities in the dolomites are reported as high as ~8 % SiO_2 (Valdiya, 1968), whereas the magnesites, in contrast, are coarsely crystalline and chemically pure, with < 1 % silica content (Fig. 4**A, C, and D)**. Mineral chemistry reveals a very low concentration of Ca in the magnesite horizons, validating our field inferences that enough Ca in the basin was not available for dolomite or limestone precipitation. Several authors tried to explain the formation of sparry magnesite through 1) intense evaporation in playa or sabkha environment (Banerjee et al., 1986; Melezhik et al., 2001)**,** 2) injection of condensed Mg-rich hydrothermal solution into the basin (Henjes-Kunst et al., 2014). In case of Kumaun magnesite, intense evaporation would result in the formation of salt species in magnesite beds along with a higher $\delta^{18}O$ value of magnesite relative to the host dolomites (Lloyd,

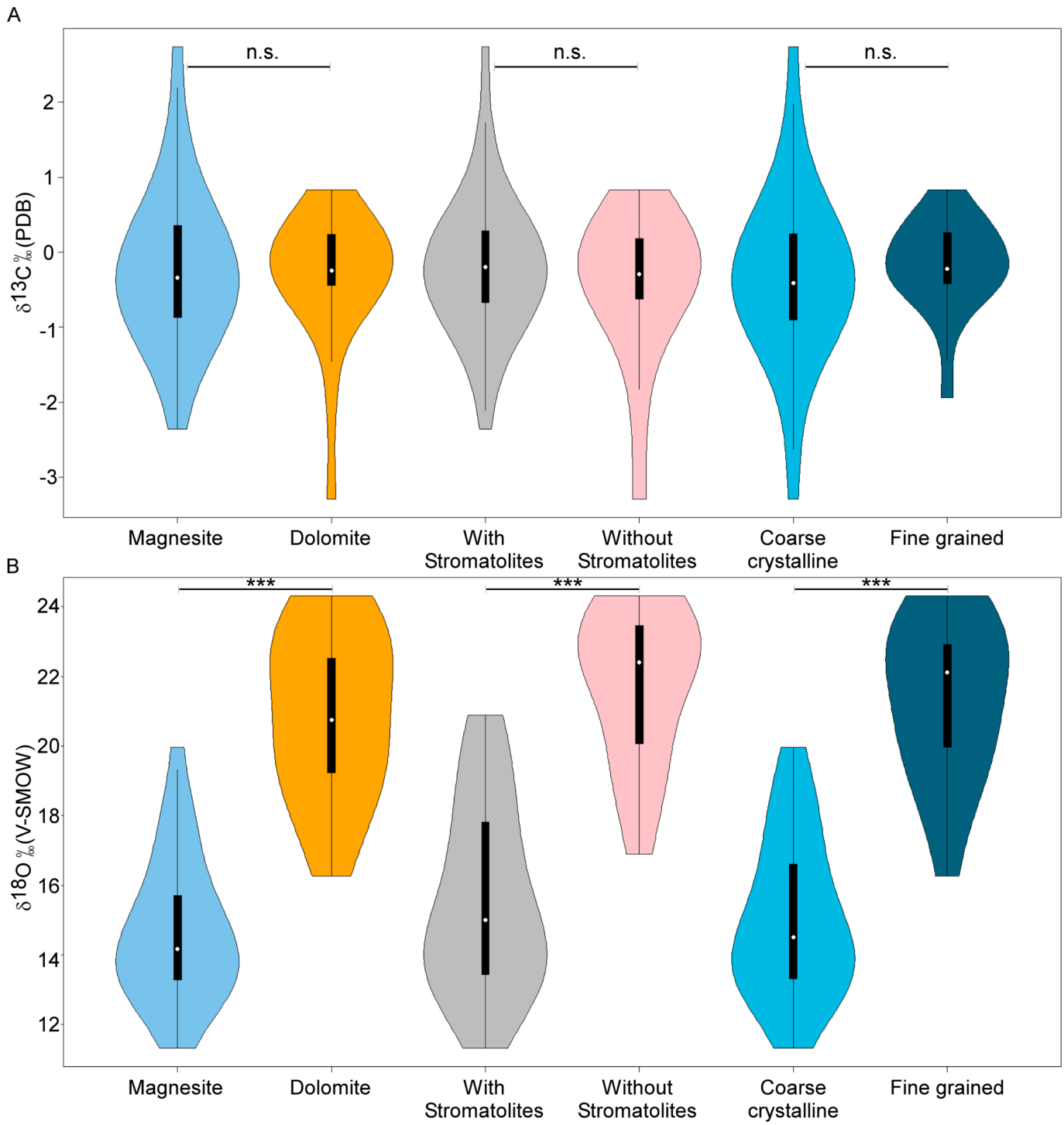

Fig. 8. Distribution of oxygen and carbon isotopic composition of the Deoban Formation. The width of the curves of the violin plot depicts the probability density of the data, i.e., proportional to the **A)** carbon isotopic compositions. **B)** oxygen isotopic composition for their respective category (labelled on the x-axis). The white dot in the middle represents the median. The box indicates the interquartile range. *** indicates a statistically significant difference between the two data sets (two-tailed *t* test, P <.001). If the difference is not significant, it is represented by n.s.

1966), neither of them was observed. The hydrothermal input is unlikely because it would require a colossal Mg-rich hydrothermal source to produce several million tons of magnesite in Kumaun (Valdiya, 1968) and other parts of the Himalayas. Even if we assume a presence of a hypothetical colossal, extremely condensed, and ultrapure Mg-rich hydrothermal source below the Deoban basin that transferred a large amount of Mg into the basin, the above assumption will result in several serious complications. We know that it is unlikely to have MgO as a free phase in the crust and upper mantle (Santos et al., 2019). Moreover, an upward transportation of Mg-rich hydrothermal fluids in the Deoban basin would also bring silicate and hydrothermal impurity to the basin (Morgan & Wandless, 1980), that is present in the path of the hydrothermal source and the Deoban basin. This will certainly contribute towards high-temperature hydrothermal minerals and metal impurity (heterogeneity) in magnesite horizons (Langmuir et al., 1997), which is not identified in Kumaun. Also, hydrothermal system would prefer

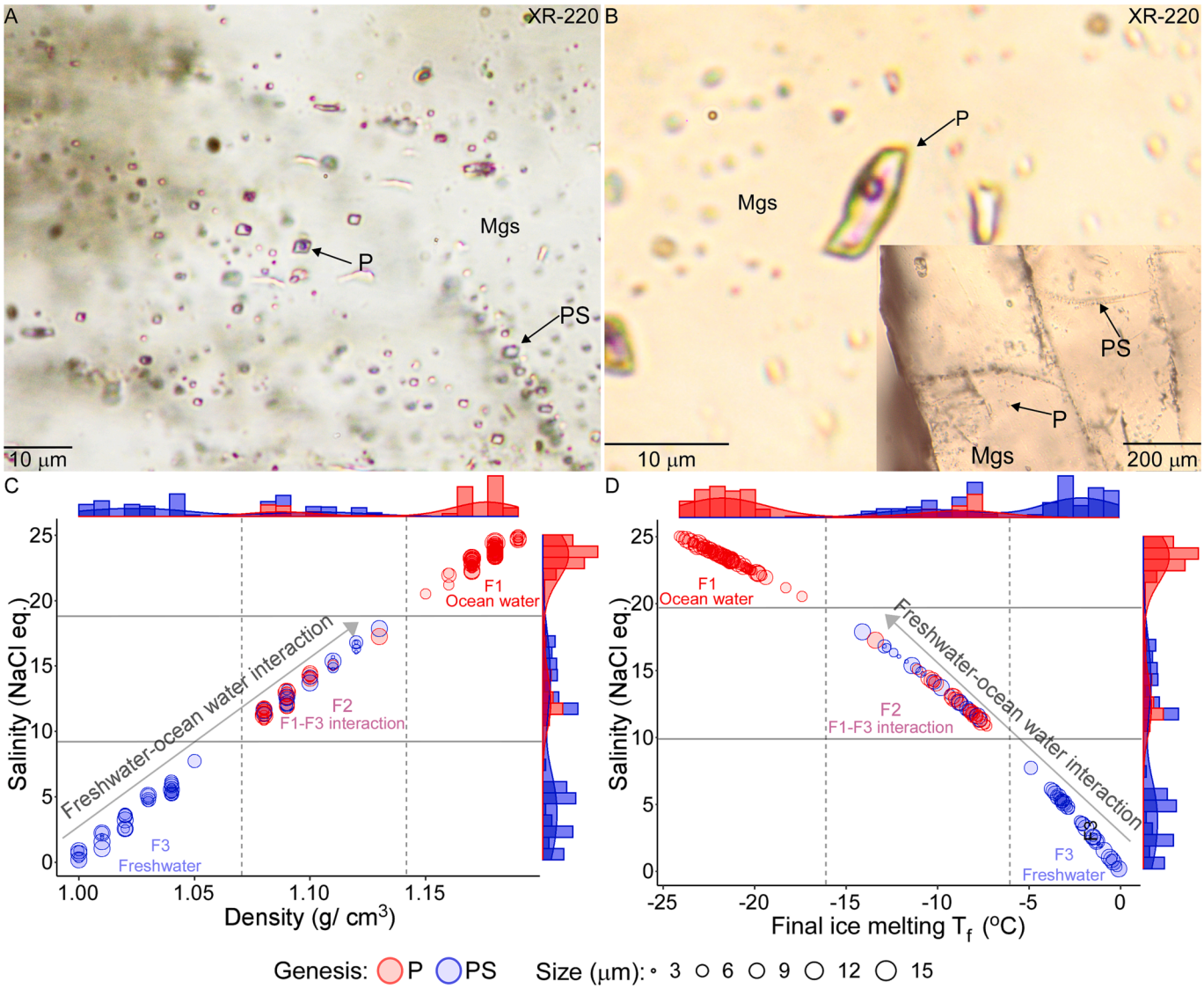

Fig. 9. Fluid inclusions characteristics. A) Red circles represent Primary (P), and blue circle represents pseudosecondary (PS) fluids in magnesite (Mgs). Different sized circle represents size of the fluid inclusions in microns. **B)** Magnified P and trails of PS fluids. **C)** Density Vs salinity variation. **D)** Final ice melting (T_f) Vs salinity variation.

mineralization in joints, fractures, and weak planes (Ledésert et al., 2010) along with associated metallic species (e.g., Pb, Zn, Cu, Mo) (Audétat et al., 2008; Glasby & Notsu, 2003; Varnavas & Papavasiliou, 2020), none of them is present in the vicinity of the study area. Chemical purity along with the absence of hydrothermal minerals and metals rules out a possible hydrothermal input. The low Ca in the basin is most plausibly related to the onset of Neoproterozoic glaciation leading to low or ceased input of ions from the frozen rivers, i.e., ions source to the basin (Martin & Whitfield, 1983). Protracted calcite-dolomite precipitation in a closed basin will eventually decrease Ca/Mg ratio in the seawater, making the basin Mg supersaturated and nutrient-deficient (i.e., Ca starved) over time, providing conditions suitable for magnesite precipitation.

The REE patterns of the dolomite and magnesite are similar to freshwater-dominated shallow marine carbonates (Liang et al., 2020), i.e., supporting the sedimentary origin of the magnesites. However, two magnesite samples from recrystallized veins had a positive Eu anomaly, possibly resulting from Eu redistribution during the recrystallization (Fig. 5). The superchondritic Y/Ho ratios of the dolomites and magnesites (Valdés-Vilchis et al., 2021), average $[Ce/Ce^*]_N$, and average $[Gd/Gd^*]_N$ are consistent with a shallow marine depositional environment (Madhavaraju & Ramasamy, 1999). The Er/Nd ratios of the dolomite and magnesite are higher than normally found in shallow marine carbonates (Madhavaraju & Ramasamy, 1999), not because of diagenesis, which decreases Er/Nd but rather indicative of an oxygenic environment (Sholkovitz et al., 1992). The same (oxygenic environment) is reflected in the low concentrations of redox-sensitive elements (e.g., U, V, Co and Cr) (Madhavaraju & Ramasamy, 1999) **(Supplementary Table S2)**. The Ce anomaly and redox-sensitive elements suggest the conditions in the Deoban basin were oxygenic, but they were insufficient to produce a strong negative Ce anomaly, as observed in the modern oceans (Wallace et al., 2017). Such weakly negative Ce anomaly is known from the shallow marine carbonates of the Tonian–Cryogenian period of the Late Neoproterozoic (Wallace et al., 2017). The same is reflected in the Deoban carbonates (magnesite and dolomite).

This oxygenic environment is possibly created by the photosynthetic stromatolites observed in the field. However, the rampant growth and increase in the size of the stromatolites **(**Fig. 1**C and** Fig. 3**B and D)** in magnesite horizons can be explained by Cope's law (Stanley, 1973) and is probably related to the adaptation of microbialites to the change in chemistry (Mg enrichment, Ca-deficient) of the basin, i.e., for binding and trapping Mg from the water column. Another strong possibility of

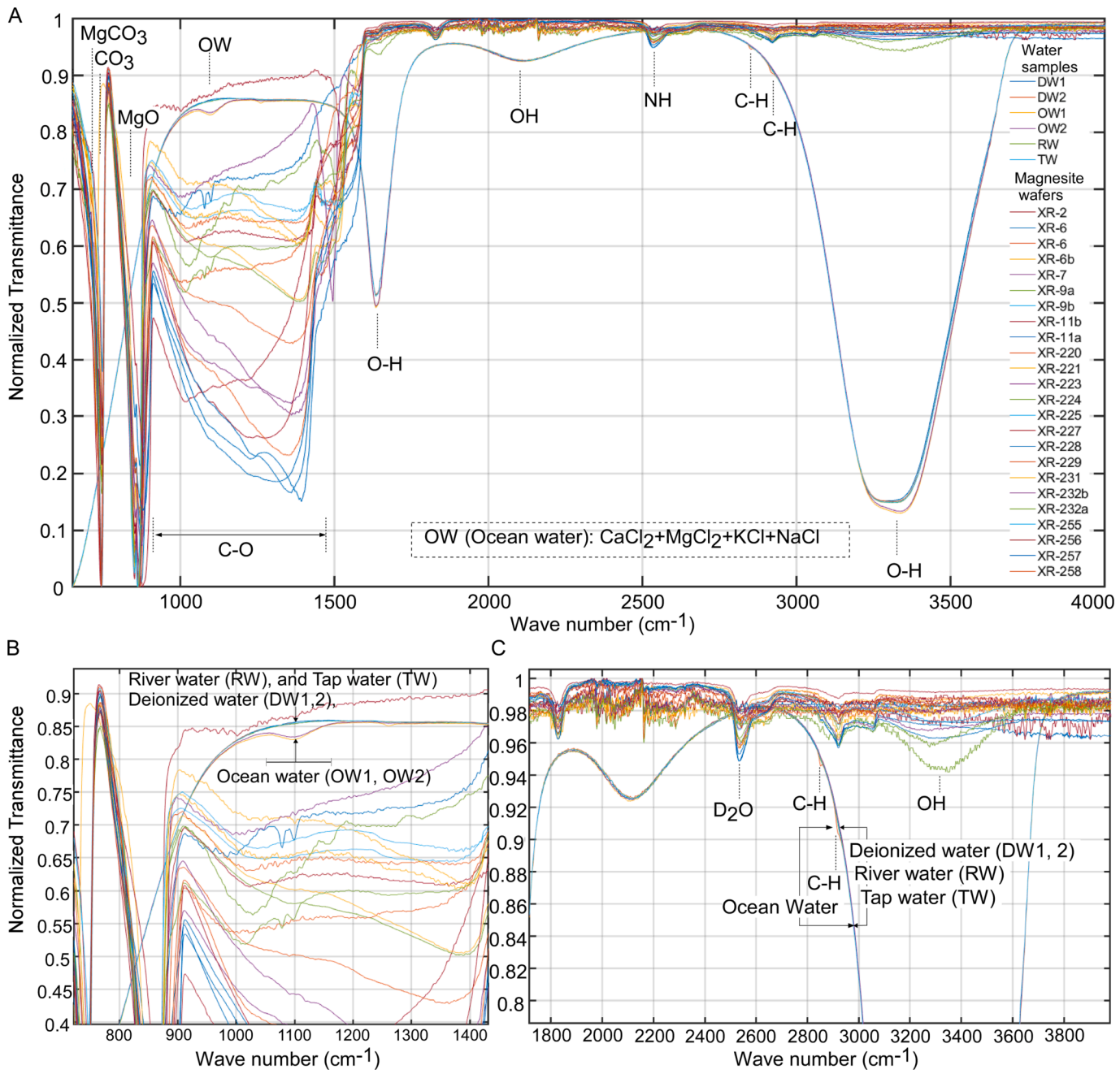

Fig. 10. Infrared characteristics. A) Infrared spectra of oceanwater (OW1 and OW2), river water (RW), filtered tap water (TW), deionized water (DW1 and DW2) and fluid-bearing magnesite wafers (XR prefixed). **B)** Oceanwater magnified region. **C)** Organic matter magnified region.

the stromatolite's population expansion is the prevalence of oligotrophic (nutrition deficient) conditions during the magnesite precipitation. Most microorganisms will hardly survive in such conditions. Only a few organisms, like stromatolites (oligotrophs), have an advantage over other species to survive and expand in nutrition-deficient (Ca-starved) environments if sunlight is available (Keupp et al., 1993).

Moreover, the absence of other microorganisms that may be predators or competitors for space and nutrition further escalates the growth of stromatolites. There is a higher possibility of a combined effect of the same as both (changes in basin chemistry and nutrition deficiency) are contemporaneous. Protracted precipitation (Ca, Mg, or both) of calcite and dolomite in a closed basin will enormously increase the oligotrophy in the basin (Mg supersaturation and Ca starved) and will initiate a positive feedback loop, i.e., more precipitation will directly result in an exponential growth of microbialites that corresponds to a rise of oxygen in the Neoproterozoic, a plausible first-order trigger for the Neoproterozoic Oxygenation Event. Molecular oxygen has played a significant role in shaping Earth's environment. Even though oxygen is the most abundant element (by weight) in the Earth's crust (Barrow, 1986), free oxygen was unavailable or only partly available during most of the Earth's history. The emergence of oxygen in the atmosphere is strongly linked to major changes in tectonics, environment, and biological evolution (Och & Shields-Zhou, 2012). Also, its presence in the oceans and atmosphere initiated planetary-scale interaction between the biosphere and environment, leading to an irreversible threshold of high oxygen levels that we see today (Och & Shields-Zhou, 2012). The oxygen level almost reached the present atmospheric level during the Neoproterozoic-Phanerozoic transition (Berner, 2006; Berner et al., 2003; Canfield, 2005; Nursall, 1959). However, the extent, timing, and drivers of the Earth's oxygenation event in the Neoproterozoic are still

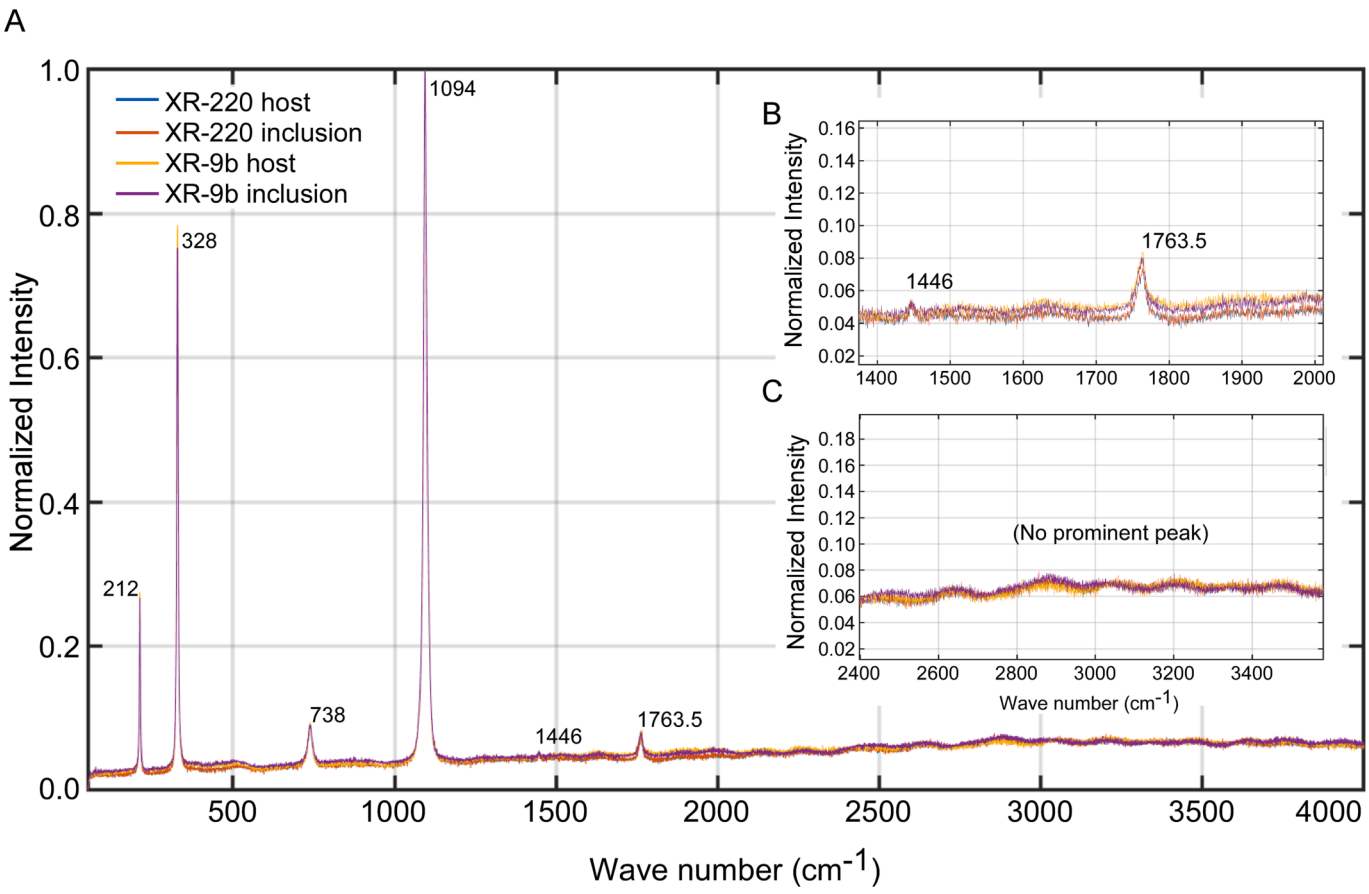

Fig. 11. Raman spectra of the fluid inclusions bearing sparry magnesite wafers. A) Characteristic Raman peaks (labelled) of the sparry magnesites from the Kumaun Himalayas. **B)** and **C)** Highlighted regions of the Raman spectra from ~1400 to 2000 and ~2400 to 4000 cm^{-1}, respectively.

controversial (Och & Shields-Zhou, 2012). Being an electron acceptor, oxygen drives the metabolism required for the growth of the advanced and complex life forms most feasibly and efficiently (Catling et al., 2005), and its accumulation in the atmosphere has forever changed the chemical conditions and biological response of the Earth (Canfield, 2005; Och & Shields-Zhou, 2012).

Thus, the Deoban basin preserves evidence of Snowball Earth induced ceased sedimentary flux, reduced nutrition supply, changes in the basin's chemistry, the response of the cyanobacterial algal mats, and the prevalence of oxygenic environment in the Neoproterozoic time. The sequence of these events would produce enormous oxygen towards the late stage of Snowball Earth glaciations—a likely first-order trigger for the Neoproterozoic Oxygenation Event. Such information is vital for understanding the poorly understood cause-and-effect relationships of the planetary-scale processes dominant during the Neoproterozoic time.

4.3. Stable isotopes track carbonate precipitation during Neoproterozoic glaciation

In the global comparison of the sparry magnesite with marine carbonates, we found the C–O isotopic composition of the worldwide sparry magnesite is remarkably similar to that of the marine carbonates (Knauth & Kennedy, 2009). The oxygen and carbon isotopic composition of the Kumaun magnesite and dolomites coherently fall within the C–O isotopic range of the marine carbonates (**Fig. 6A and Fig. 7**). The carbon isotopic composition does not show a statistically significant difference between the dolomite and magnesite, presence or absence of stromatolite, and if coarsely crystalline or fine-grained (two-tailed *t* test, $P > .05$) (**Fig. 6B and Fig. 8A**). The carbon isotopic composition remained nearly constant during the upward transition of dolomites (~−3.2–0.8 ‰) to magnesites (~−2.3–2.7 ‰) (**Fig. 6A**), suggesting the biological uptake and release of inorganic carbon and air-sea-CO_2 exchange in the Deoban basin were stable during magnesite and dolomite precipitation (Cheng et al., 2019). The presence of organic materials can lower the carbon isotopic composition of carbonates during low-grade metamorphism (Kiran et al., 2022), but constant values irrespective of the presence or absence of organic material suggest that post-depositional carbon isotopic fractionation was limited. The carbon isotopic composition of the carbonates formed from hydrothermal or deep magmatic fluids have significantly lower (~−5 ‰ or lower) $\delta^{13}C$ values. Such lower values are not found in our results, further validating that the Deoban carbonates are unrelated to hydrothermal or magmatic fluids (Horton et al., 2012). Also, the carbon isotopes show enrichment of ^{13}C during intense evaporation leading to higher (~19.8 to 34.9 ‰) values of $\delta^{13}C$ (Stiller et al., 1985). However, in our case, the $\delta^{13}C$ values are significantly lower (~−3.2–0.8 ‰) and remained constant during the transition from dolomites to magnesite, suggesting that these magnesite and dolomite are unrelated to evaporation in lagoon, sabkha or playa lake as anticipated by Valdiya, 1968. Altogether, the close isotopic similarity of the sparry magnesites with marine carbonates hints toward their sedimentary origin.

However, a statistically significant difference exists between the temperature-sensitive oxygen isotopic composition of the magnesite and dolomite (two tailed *t* test, $P < .001$) (**Fig. 6B and Fig. 8B**). Since all magnesites are stromatolite-bearing and coarsely crystalline, the same is reflected in the results, i.e., coarsely crystalline stromatolite-bearing carbonates (mainly magnesite) has lower $\delta^{18}O$ values relative to fine-grained non-stromatolite-bearing ones (mainly dolomite) (two tailed *t* test, $P < .001$) (**Fig. 8B**). There are several factors which can affect primary oxygen isotopic composition that may result in the lowering of

$\delta^{18}O$ values, such as 1) Kinetic processes (metabolism, photosynthesis, and respiration) (Auclair et al., 2003), and 2) Burial diagenesis (Colombie et al., 2011). However, the kinetic changes appear to be limited (~2 ‰) between stromatolites-bearing (average ~19 ‰) and non-bearing dolomites (average ~22 ‰). Although, there are several uncertainties (mentioned above) that may influence oxygen isotope values, however, the possibility of precipitation of the magnesite from glacial meltwater (highly depleted in ^{18}O) cannot be avoided that can potentially produce a significantly large difference (~8 ‰) in $\delta^{18}O$ values between magnesite and dolomite which is unlikely to occur due to kinetic processes or diagenesis because the stromatolite bearing magnesites (average ~15 ‰) are much more depleted in $\delta^{18}O$ values than stromatolite-bearing dolomite (average ~19 ‰) **(Supplementary Table S4)**.

Since the Deoban Formation formed during the Cryogenian period, this large variation in $\delta^{18}O$ between magnesite and dolomites is likely a result of magnesite precipitation from glacial meltwater ($\delta^{18}O$ ~-25 ‰) strongly depleted (~–25 ‰) $\delta^{18}O$ value (Morley et al., 2005). The close isotopic (C–O) similarity of the Himalayan sparry magnesites with marine carbonates also indicates that the magnesites are sedimentary in origin and were likely formed in freshwater (glacial meltwater) dominated shallow marine carbonate platforms ideal for cyanobacterial growth. Such freshwater pools suitable for cyanobacterial growth and evolution existed during the Cryogenian periods of the Neoproterozoic time (Sánchez-Baracaldo, 2015).

4.4. Saline water and freshwater fluid inclusions in sparry magnesite

The density and salinity of aqueous fluid inclusions fall from F1 to F3 **(Fig. 9C and D)**. This progressive fall in both density and salinity could be attributed to 1) the mixing of hydrothermal basinal fluids (Kilias et al., 2006), 2) burial and long residence time, and 3) the presence of saline fluids in deeper zones (Sharma, 2006). The mixing of hydrothermal fluids can be discounted as it would produce chemical heterogeneity in the magnesite horizons and dominance of hydrothermal gas species in fluid inclusions (James et al., 2014)**;** neither of the two is observed. Increased salinity due to burial and long residence times can be discounted because the chemically pure magnesite crystals contain insufficient salt to enhance the salinity **(Supplementary Table S1)**. Saline fluids derived from deeper zones can be discounted because the stromatolite-bearing magnesites crystallized in an oxic, shallow marine environment **(Fig. 5, Supplementary Table S2)** (Banerjee et al., 1986). Since the Neoproterozoic era experienced multiple Snowball Earth glacial Events, the possible explanation for the density and salinity variation is the slow release of ^{18}O depleted glacial meltwater from the overlying or surrounding glaciers. Another contributing factor could be the meltwater from the previous Snowball Earth Events. In both cases, stratification of the water in the basin can occur—the upper layer consists of glacial meltwater, and the lower layer consists of saline oceanwater (Yang et al., 2017). In such a situation, the shallow marine environment will be dominated by freshwater. Most probably, the sparry magnesite in the Himalayas precipitated from such freshwater pools. The F3 fluids are remnants of the same. After the Neoproterozoic Snowball Earth Events, the two layers were homogenized (maximum $\sim 5 \times 10^4$ years) (Yang et al., 2017), and F1 fluid possibly represents the remnants of the well-mixed oceanwater in the pore space of magnesite precipitate after the deglaciation event. The F2 fluids represent the intermediate stage between F1 and F3, i.e., preserving the freshwater and oceanwater interaction in the pore space **(Fig. 9C and D)**. Microthermometry and fluid modelling suggest the presence of $MgCl_2$-$CaCl_2$-NaCl-KCl salt complexes in the fluid inclusions. Similar salt complexes have been identified from fluid inclusions of the sparry magnesites from Kumaun (Sharma, 2006) and other parts of the world (Kilias et al., 2006). This salt complex is best preserved in F1 fluid inclusions and is similar in composition to the salts in seawater. To verify the same, we performed the spectroscopic analysis.

4.5. Neoproterozoic ocean and freshwater droplets in sparry magnesite

When fluid inclusions bearing wafers of the sparry magnesite free from cracks and fractures were analyzed by ATR-FTIR **(Supplementary Table S6)**, an intense band at ~740–745 cm^{-1}, ~850–852 cm^{-1}, and ~860–890 cm^{-1} revealed the presence of $MgCO_3$ (Kupwade-Patil et al., 2018), CO_3 (Gopinath & Gunasekaran, 2018; Yuniati et al., 2019), and MgO (Gopinath & Gunasekaran, 2018; Yuniati et al., 2019), respectively **(Fig. 10, A–C)**. These bands confirm our petrological results, i.e., the presence of magnesite. Infrared spectroscopy is a powerful tool that can detect a minor amount of silicate mineral impurities, the absence of any other absorption in the region (600 to 900 cm^{-1}), further validates the chemical purity of the sparry magnesite. Such chemically pure carbonate is nearly impossible to form through a hydrothermal source and is very hard to precipitate in an open basin as it would contain a small quantity of clay and quartz associated with the precipitated carbonates. The infrared spectroscopy elucidates the poorly understood sedimentation flux and ceased sedimentation during the Neoproterozoic glacial events.

Like the sedimentation flux, the information about the primitive life in the Precambrian oceans is poorly known mainly because of poor preservation, metamorphic alteration, and insufficient criteria for microbial identification other than isotopic and morphological similarities (Altermann, 2002). In such a situation, infrared spectra can provide vital information about the organic matter and structure of primitive life. Such signatures of organic material, i.e., the presence of N–H (~2540 cm^{-1}) and C–H bonds (~2850 and 2920 cm^{-1}) (Rodrigues et al., 2013), were detected in the sparry magnesites of the Kumaun **(Fig. 10A–C)**. This absorption possibly corresponds to the peptide bonds of the cyanobacterial stromatolites identified in the field (Altermann, 2002). The peptides are the fundamental building blocks of life, and their identification may hints toward the molecular structure of the primitive microbial life thriving in the Precambrian oceans.

The water molecules (OH bonds) in the sparry magnesite correspond to the IR absorption at ~1634, ~2000–2200, and ~3000–3500 cm^{-1} (Friedman, 1969). This absorption arises from water-bearing fluid inclusions (F1, F2, and F3) within magnesite. The detection of water confirms that the sparry magnesite was formed in a water-bearing environment like a sedimentary basin. The same information was obtained from our field, REE, and isotopic results. Further, the identified salt complex ($MgCl_2$, NaCl, KCl, $MgSO_4$, and $CaCl_2$) during microthermometry was verified through ~1050–1170 cm^{-1} (centred on ~1100 cm^{-1}) absorption. This absorption corresponds to the salt species (mentioned above) present in oceanwater and distinguishes sea or oceanwater from freshwater (Friedman, 1969). The presence of ~1100 cm^{-1} absorption in sparry magnesite indicates the presence of seawater (F1), confirming the sparry magnesite was precipitated from the Neoproterozoic sea. The F1 fluid inclusions are remnants of the Neoproterozoic sea, F3 represents freshwater from glacial discharge, and F2 represent freshwater-seawater interaction in pore space. Raman spectroscopy provided no additional information. Peaks at ~212, ~328, and ~1094 cm^{-1} corresponded to magnesite, and at ~1446 and ~1763 cm^{-1} corresponded to organic bonds, e.g., C≡C or C—OH bonds (Batuev et al., 1960). Since water and salt species are weak Raman scatterer, those peaks were not identified **(Fig. 11, A–C) (Supplementary Table S7)**.

Our spectroscopic results align with our other analyses and confirm the sparry magnesite is of sedimentary in origin. Identification of preserved paleo-ocean/ sea is rarely seen in the literature because fine-grained carbonates are insufficient in trapping fluid inclusions. Sparry magnesite is a rare time capsule of the paleo-oceans/ seas and can potentially provide direct information about the oceanographic parameters (chemistry, isotopic composition, salinity, alkalinity, dissolved oxygen, and pH) of the paleo-oceans. These parameters can potentially provide first-hand information on the changes in chemistry, isotopic composition, and the most important oxygen levels in the paleo oceans,

which are directly related to the oxygenation of the Earth, a primary driver for biological evolution. Until now, the above paleo-oceanographic parameters were inferred, calculated, or modelled because no archives of paleo oceans were identified, necessitating reliance on indirect methods. Direct information from trapped paleo ocean droplets can enhance our understanding of the Precambrian ocean's chemistry, physiochemical conditions, and associated life forms, which will unravel more about the poorly understood environment, oxygenation, and biological evolution of the Precambrian Earth.

5. Conclusions

Our field, REE, isotopic, and spectroscopic results strongly suggest that the sparry magnesites of the Kumaun Himalayas were precipitated from the Neoproterozoic sea (Tiwari & Pant, 2009; Valdiya, 1968), plausibly Proto-Tethys (Zhang et al., 2018). Such chemically pristine magnesite precipitation would only be possible if the calcium input and other terrigenous impurities (e.g., clay and quartz) to the Deoban Basin were interrupted for a long period, probably due to the freezing of the rivers (the source of dissolved Ca and other products of weathering) during the Neoproterozoic glaciation. The sequence of events that led to the preservation of droplets of Neoproterozoic Seawater in the magnesite crystals and related oxygenation is envisaged to be as follows:

1) The Neoproterozoic glaciation restricted the riverine input of cations into the Deoban Basin, but carbonate continued to precipitate from the shallow marine environment dominated by glacial meltwater. ***2)*** Protracted precipitation of calcite-dolomite decreased the Ca/Mg ratio in the closed basin, eventually depleting Ca and concentrating Mg to such an extent that magnesite began to precipitate. ***3)*** With the fall of Ca (nutrition deficient), the basin became increasingly oligotrophic, promoting the growth of large stromatolites, which were probably involved in the binding and trapping of Mg from the water column. ***4)*** The rampant growth of photosynthesizing stromatolites created an oxygenic environment by releasing enormous amounts of oxygen into the atmosphere. ***5)*** The magnesite precipitates preserved the glacial meltwater (from which magnesite precipitated), well-mixed oceanwater after deglaciation, and their interaction in the pore space. The same is trapped as fluid inclusions within the sparry magnesites of the Kumaun Himalayas.

The Deoban Basin preserves evidence that long-lived glacial events produce significant chemical and biological changes in the oceans that facilitate magnesite precipitation and enhance the growth of cyanobacteria. These magnesite precipitates can potentially trap paleo-oceanwater in pore space during crystallization. Continued precipitation in a closed basin initiates a chain reaction that directly contributes to high oxygen production in the late stage of the glacial event (magnesitization). The rampant growth of microbialites in the magnesite beds of Kumaun and other similar locations are potential first-order triggers of the Neoproterozoic Oxygenation Event, leading to rapid biodiversification, the Cambrian Explosion.

Declaration of Competing Interest

The authors declare that they have no known competing financial interests or personal relationships that could have appeared to influence the work reported in this paper.

Data availability

All data files are available in the Supplementary Tables

Acknowledgement

The authors express their sincere gratitude to Dr. Frances Westall for the editorial handling, and the anonymous reviewers are thanked for their constructive inputs that improved the manuscript. The authors express their gratitude to Prof. Ian S. Williams and Prof. Brian F. Windley for the helpful discussion, constructive suggestions, and corrections in the manuscript. PCA acknowledges CSIR-NET for the PhD fellowship and Dr. Harish Bisht and Vikas Arya for providing their support during the fieldwork. MSK acknowledges the partial financial support for analysis through JSPS KAKENHI grant numbers JP15H05831 and 20KK0081. CN acknowledges the Indian Institute of Science for post-doctoral support. Dr. Sambuddha Mishra is thanked for providing the ocean water sample to compare the IR spectrum. AFMM at IISc is acknowledged for providing the EPMA facility. Dr. Chiranjeeb Chatterjee is thanked for providing aid during the EPMA analysis. MSK acknowledges the help rendered by Rikako Imanaka for the trace element analysis.

Appendix A. Supplementary materials

Supplementary data to this article can be found online at https://doi.org/10.1016/j.precamres.2023.107129.

References

Aharon, P., 1988. A stable-isotope study of magnesites from the Rum Jungle Uranium Field, Australia: Implications for the origin of strata-bound massive magnesites. Chem. Geol. 69, 127–145.
Alcott, L.J., Mills, B.J.W., Poulton, S.W., 2019. Stepwise Earth oxygenation is an inherent property of global biogeochemical cycling. Science (80-.). 366, 1333–1337.
Altermann, W., 2002. The evolution of life and its impact on sedimentation. In: PrecAmbriAn SedimentAry Environments: A Modern ApproAch to Ancient DepositionAl Systems. Wiley Online Library, pp. 15–32.
Anders, E., Grevesse, N., 1989. Abundances of the elements: Meteoritic and solar. Geochim. Cosmochim. Acta 53, 197–214.
Auclair, A.C., Joachimski, M.M., Lécuyer, C., 2003. Deciphering kinetic, metabolic and environmental controls on stable isotope fractionations between seawater and the shell of Terebratalia transversa (Brachiopoda). Chem. Geol. 202, 59–78. https://doi.org/10.1016/S0009-2541(03)00233-X.
Audétat, A., Pettke, T., Heinrich, C.A., Bodnar, R.J., 2008. Special paper: The composition of magmatic-hydrothermal fluids in barren and mineralized intrusions. Econ. Geol. https://doi.org/10.2113/gsecongeo.103.5.877.
Azim Zadeh, A.M., Ebner, F., Jiang, S.Y., 2015. Mineralogical, geochemical, fluid inclusion and isotope study of Hohentauern/Sunk sparry magnesite deposit (Eastern Alps/Austria): implications for a metasomatic genetic model. Mineral. Petrol.
Azmi, R.J., Paul, S.K., 2004. Discovery of Precambrian-Cambrian boundary protoconodonts from the Gangolihat Dolomite of Inner Kumaun Lesser Himalaya: Implication on age and correlation. Curr, Sci.
Bajaj, P., Arya, P.C., 2021. Evolution and spread of SARS-CoV-2 likely to be affected by climate. Clim. Chang. Ecol. 1, 100005.
Banerjee, D.M., Schidlowski, M., Arneth, J.D., 1986. Genesis of upper Proterozoic-Cambrian phosphorite deposits of India: isotopic inferences from carbonate fluorapatite, carbonate and organic carbon. Precambrian Res. 33, 239–253.
Barrow, J.D., 1986. The anthropic cosmological principle. Oxford Univ, Press.
Batuev, M.I., Akhrem, A.A., Matveeva, A.D., 1960. Raman-spectrum investigation of some acetylenic alcohols and their acetic esters. Bull. Acad. Sci. USSR. Div. Chem. Sci. 9, 2037–2042.
Berner, R.A., 2006. GEOCARBSULF: a combined model for Phanerozoic atmospheric O2 and CO2. Geochim. Cosmochim. Acta 70, 5653–5664.
Berner, R.A., Beerling, D.J., Dudley, R., Robinson, J.M., Wildman Jr, R.A., 2003. Phanerozoic atmospheric oxygen. Annu. Rev. Earth Planet. Sci. 31, 105–134.
Bodnar, R.J., 1993. Revised equation and table for determining the freezing point depression of H2O-Nacl solutions. Geochim. Cosmochim. Acta.
Bodnar, R.J., 2006. How melted rock migrates. Science (80-.) 314, 934–935.
Canfield, D.E., 2005. The early history of atmospheric oxygen: homage to Robert M. Garrels. Annu. Rev. Earth Planet. Sci. 33, 1–36.
Canfield, D.E., Poulton, S.W., Narbonne, G.M., 2007. Late-Neoproterozoic deep-ocean oxygenation and the rise of animal life. Science (80-.). 315, 92–95.
Catling, D.C., Glein, C.R., Zahnle, K.J., McKay, C.P., 2005. Why O2 is required by complex life on habitable planets and the concept of planetary" oxygenation time". Astrobiology 5, 415–438.
Cheng, L., Normandeau, C., Bowden, R., Doucett, R., Gallagher, B., Gillikin, D.P., Kumamoto, Y., McKay, J.L., Middlestead, P., Ninnemann, U., et al., 2019. An international intercomparison of stable carbon isotope composition measurements of dissolved inorganic carbon in seawater. Limnol. Oceanogr. Methods 17, 200–209.
Colombie, C., Lécuyer, C., Strasser, A., 2011. Carbon-and oxygen-isotope records of palaeoenvironmental and carbonate production changes in shallow-marine carbonates (Kimmeridgian, Swiss Jura). Geol. Mag. 148, 133–153.
Etienne, J.L., Allen, P.A., le Guerroué, E., Heaman, L., Ghosh, S.K., Islam, R., 2011. Chapter 31 the blaini formation of the lesser himalaya, NW India. Geol Soc. London, Mem. 36, 347–355.
Fairchild, I.J., Kennedy, M.J., 2007. Neoproterozoic glaciation in the Earth System. J. Geol. Soc. London. 164, 895–921.
Friedman, D., 1969. Infrared characteristics of ocean water (15–15 μ). Appl. Opt.

Garber, R.A., Harris, P.M., Borer, J.M., 1990. Occurrence and significance of magnesite in Upper Permian (Guadalupian) Tansill and Yates Formations, Delaware Basin, New Mexico1. Am. Assoc. Pet. Geol. Bull. 74, 119–134.
Glasby, G.P., Notsu, K., 2003. Submarine hydrothermal mineralization in the Okinawa Trough, SW of Japan: an overview. Ore Geol. Rev. 23, 299–339.
Gopinath, D., Gunasekaran, S., 2018. The FTIR spectra of raw magnesite and sintered magnesite. Int. J. Trend Sci. Res. Dev.
Halevy, I., Bachan, A., 2017. The geologic history of seawater pH. Science (80-.) 355, 1069–1071.
Henjes-Kunst, F., Prochaska, W., Niedermayr, A., Sullivan, N., Baxter, E., 2014. Sm-Nd dating of hydrothermal carbonate formation: An example from the Breitenau magnesite deposit (Styria, Austria). Chem. Geol.
Herbei, M., Ciolac, V., Smuleac, A., Ciolac, L., 2010. Georeferencing of topographical maps using the software ArcGIS. Res. J. Agric. Sci. 42, 595–606.
Herrero, M.J., Martín-Pérez, A., Alonso-Zarza, A.M., Gil-Peña, I., Meléndez, A., Martín-García, R., 2011. Petrography and geochemistry of the magnesites and dolostones of the Ediacaran Ibor Group (635 to 542Ma), Western Spain: Evidences of their hydrothermal origin. Sediment. Geol.
Hofmann, M., Linnemann, U., Rai, V., Becker, S., Gärtner, A., Sagawe, A., 2011. The India and South China cratons at the margin of Rodinia—Synchronous Neoproterozoic magmatism revealed by LA-ICP-MS zircon analyses. Lithos 123, 176–187.
Horton, T.W., Atkinson, L., Oze, C., others, 2012. Hydrothermal carbonate geochemistry of the Ngatamariki subsurface reservoir, New Zealand, in: Proceedings of the Thirty-Seventh Workshop on Geothermal Reservoir Engineering, Stanford, California. pp. 1–8.
James, R.H., Green, D.R.H., Stock, M.J., Alker, B.J., Banerjee, N.R., Cole, C., German, C. R., Huvenne, V.A.I., Powell, A.M., Connelly, D.P., 2014. Composition of hydrothermal fluids and mineralogy of associated chimney material on the East Scotia Ridge back-arc spreading centre. Geochim. Cosmochim. Acta.
Joachimski, M.M., van Geldern, R., Breisig, S., Buggisch, W., Day, J., 2004. Oxygen isotope evolution of biogenic calcite and apatite during the Middle and Late Devonian. Int. J. Earth Sci.
Joshi, P., Pant, P.D., 2017. Petrography and oxygen, carbon isotopic signatures of the magnesite from Bageshwar District, Kumaun Himalaya focusing on genesis and depositional environment of magnesite. Himal. Geol.
Kazmierczak, J., Altermann, W., 2002. Neoarchean biomineralization by benthic cyanobacteria. Science 298-5602, 2351.
Keupp, H., Jenisch, A., Herrmann, R., Neuweiler, F., Reitner, J., 1993. Microbial carbonate crusts-a key to the environmental analysis of fossil spongiolites? Facies 29, 41–54.
Kilias, S.P., Pozo, M., Bustillo, M., Stamatakis, M.G., Calvo, J.P., 2006. Origin of the Rubian carbonate-hosted magnesite deposit, Galicia, NW Spain: Mineralogical, REE, fluid inclusion and isotope evidence. Miner. Depos. https://doi.org/10.1007/s00126-006-0075-5.
Kiran, S., Satish-Kumar, M., Nakamura, Y., Hokada, T., 2022. Comparison between Raman spectra of carbonaceous material and carbon isotope thermometries in low-medium grade meta-carbonates: Implications for estimation of metamorphic temperature condition. Precambrian Res. 374, 106656.
Kirschvink, J.L., Gaidos, E.J., Bertani, L.E., Beukes, N.J., Gutzmer, J., Maepa, L.N., Steinberger, R.E., 2000. Paleoproterozoic snowball Earth: Extreme climatic and geochemical global change and its biological consequences. Proc. Natl. Acad. Sci. 97, 1400–1405.
Knauth, L.P., Kennedy, M.J., 2009. The late Precambrian greening of the Earth. Nature. https://doi.org/10.1038/nature08213.
Kralik, M., Hoefs, J., 1978. Die Isotopenzusammensetzung der Karbonate in der Magnesitlagerstätte Eugui (Westpyrenäen). TMPM Tschermaks Mineral. und Petrogr. Mitteilungen. https://doi.org/10.1007/BF01081419.
Kupwade-Patil, K., Palkovic, S.D., Bumajdad, A., Soriano, C., Büyüköztürk, O., 2018. Use of silica fume and natural volcanic ash as a replacement to Portland cement: Micro and pore structural investigation using NMR, XRD, FTIR and X-ray microtomography. Constr. Build. Mater. https://doi.org/10.1016/j.conbuildmat.2017.09.165.
Langmuir, C., Humphris, S., Fornari, D., Van Dover, C., Von Damm, K., Tivey, M.K., Colodner, D., Charlou, J.-L., Desonie, D., Wilson, C., et al., 1997. Hydrothermal vents near a mantle hot spot: the Lucky Strike vent field at 37 N on the Mid-Atlantic Ridge. Earth Planet. Sci. Lett. 148, 69–91.
Ledésert, B., Hebert, R., Genter, A., Bartier, D., Clauer, N., Grall, C., 2010. Fractures, hydrothermal alterations and permeability in the Soultz Enhanced Geothermal System. Comptes Rendus Geosci. 342, 607–615.
Liang, T., Bao, Z., Zhu, X., Guo, Y., Li, J., Jones, B., 2020. Rare earth elements in dolostones and limestones from the Mesoproterozoic Gaoyuzhuang Formation, North China: Implications for penecontemporaneous dolomitization. J. Asian Earth Sci. 196, 104374.
Lloyd, R.M., 1966. Oxygen isotope enrichment of sea water by evaporation. Geochim. Cosmochim. Acta 30, 801–814.
Lugli, S., 2001. Timing of post-depositional events in the Burano Formation of the Secchia valley (Upper Triassic, Nothern Apennines), clues from gypsum-anhydrite transitions and carbonate metasomatism. Sediment. Geol. https://doi.org/10.1016/S0037-0738(00)00174-3.
Luo, G., Ono, S., Beukes, N.J., Wang, D.T., Xie, S., Summons, R.E., 2016. Rapid oxygenation of Earth's atmosphere 2.33 billion years ago. Sci. Adv. 2, e1600134.
Madhavaraju, J., Ramasamy, S., 1999. Rare earth elements in limestones of Kallankurichchi formation of Ariyalur Group, Tiruchirapalli Cretaceous. Tamil Nadu. J. Geol. Soc. India 54, 291–301.
Martin, J.-M., Whitfield, M., 1983. The significance of the river input of chemical elements to the ocean. In: Trace Metals in Sea Water. Springer, US, Boston, MA, pp. 265–296.
McNeil, B., Morris, E., 1992. The preparation of double-polished fluid inclusion wafers from friable, water-sensitive material. Mineral. Mag. https://doi.org/10.1180/minmag.1992.056.382.18.
Melezhik, V.A., Fallick, A.E., Medvedev, P.V., Makarikhin, V.V., 2001. Palaeoproterozoic magnesite: Lithological and isotopic evidence for playa/sabkha environments. Sedimentology. https://doi.org/10.1046/j.1365-3091.2001.00369.x.
Misch, D., Pluch, H., Mali, H., Ebner, F., Huang, H., 2018. Genesis of giant Early Proterozoic magnesite and related talc deposits in the Mafeng area, Liaoning Province, NE China. J. Asian Earth Sci. 5, 6. https://doi.org/10.1016/j.jseaes.2018.04.005.
Morgan, J.W., Wandless, G.A., 1980. Rare earth element distribution in some hydrothermal minerals: evidence for crystallographic control. Geochim. Cosmochim. Acta 44, 973–980.
Morley, D.W., Leng, M.J., Mackay, A.W., Sloane, H.J., 2005. Late glacial and Holocene environmental change in the Lake Baikal region documented by oxygen isotopes from diatom silica. Glob. Planet. Change 46, 221–233.
Mukherjee, P.K., Jain, A.K., Singhal, S., Singha, N.B., Singh, S., Kumud, K., Seth, P., Patel, R.C., 2019. U-Pb zircon ages and Sm-Nd isotopic characteristics of the Lesser and Great Himalayan sequences, Uttarakhand Himalaya, and their regional tectonic implications. Gondwana Res 75, 282–297.
Negi, M., Saha, S., Ghosh, S.K., Rai, S.K., 2022. Provenance and sedimentation age of the Proterozoic clastic succession of the Garhwal-Kumaon Lesser Himalaya, NW-India: Clues from U-Pb zircon and Sr–Nd isotopes. Geol. J.
Neo, N., Yamazaki, S., Miyashita, S., 2009. Data report: bulk rock compositions of samples from the IODP Expedition 309/312 sample pool, ODP Hole 1256D. Proc. Integr. Ocean Drill. Progr. 309.
Nursall, J.R., 1959. Oxygen as a prerequisite to the origin of the Metazoa. Nature 183, 1170–1172.
Och, L.M., Shields-Zhou, G.A., 2012. The Neoproterozoic oxygenation event: Environmental perturbations and biogeochemical cycling. Earth-Science Rev. 110, 26–57.
Parente, C.V., Ronchi, L.H., Sial, A.N., Guillou, J.J., Arthaud, M.H., Fuzikawa, K., Veríssimo, C.U.V., 2004. Geology and geochemistry of paleoproterozoic magnesite deposits (~1.8Ga), state of Ceará, northeastern Brazil. Carbon. Evaporites. 8 https://doi.org/10.1007/BF03175194.
Peck, W.H., Eppich, G.R., 2019. The kilmar magnesite deposits: Evaporitic metasediments in the Grenville supergroup, Morin Terrane, Quebec. Minerals. https://doi.org/10.3390/min9090554.
Pierrehumbert, R.T., Abbot, D.S., Voigt, A., Koll, D., 2011. Climate of the Neoproterozoic. Annu. Rev. Earth Planet. Sci. 39, 417–460.
Raha, P.K., Sastry, M.V.A., 1982. Stromatolites and Precambrian stratigraphy in India. Precambrian Res. 18, 293–318.
Reed, F.S., Mergner, J.L., 1953. Preparation of Rock Thin Sections. Amer. Miner.
Rodrigues, N.V.S., Cardoso, E.M., Andrade, M.V.O., Donnici, C.L., Sena, M.M., 2013. Analysis of seized cocaine samples by using chemometric methods and FTIR spectroscopy. J. Braz. Chem. Soc. 24, 507–517.
Sahoo, S.K., Planavsky, N.J., Kendall, B., Wang, X., Shi, X., Scott, C., Anbar, A.D., Lyons, T.W., Jiang, G., 2012. Ocean oxygenation in the wake of the Marinoan glaciation. Nature 489, 546–549.
Sánchez-Baracaldo, P., 2015. Origin of marine planktonic cyanobacteria. Sci. Rep. 5, 1–10.
Santos, S.S.M., Marcondes, M.L., Justo, J.F., Assali, L.V.C., 2019. Stability of calcium and magnesium carbonates at Earth's lower mantle thermodynamic conditions. Earth Planet. Sci. Lett. 506, 1–7.
Satish-Kumar, M., Sashidharan, K., Abe, M., 2021a. A new inlet system for microscale carbon and oxygen stable isotope analysis using dual isotope ratio mass spectrometer at Niigata University (Geology). Sci. reports Niigata Univ. 36, 21–42.
Satish-Kumar, M., Shirakawa, M., Imura, A., Otsuji-Makino, N., Imanaka-Nohara, R., Malaviarachchi, S.P.K., Fitzsimons, I.C.W., Sajeev, K., Grantham, G.H., Windley, B. F., et al., 2021b. A geochemical and isotopic perspective on tectonic setting and depositional environment of Precambrian meta-carbonate rocks in collisional orogenic belts. Gondwana Res. 96, 163–204.
Schelling, D., 1992. The tectonostratigraphy and structure of the eastern Nepal Himalaya. Tectonics 11, 925–943.
Schulz, O., Vavtar, F., 1977. Sedimentary magnesite fabrics within the sparry magnesite deposit Hochfilzen (Tyrol). Time-and Strata-Bound Ore Deposits. Springer 260–270.
Sharma, R., 2006. Nature of fluids and regional implications for Lesser Himalayan carbonates and associated mineralization. J. Geochemical Explor. 89, 363–367.
Sholkovitz, E.R., Shaw, T.J., Schneider, D.L., 1992. The geochemistry of rare earth elements in the seasonally anoxic water column and porewaters of Chesapeake Bay. Geochim. Cosmochim. Acta 56, 3389–3402. https://doi.org/10.1016/0016-7037(92)90386-W.
Singh, S., 2019. Protracted zircon growth in migmatites and in situ melt of Higher Himalayan Crystallines: U–Pb ages from Bhagirathi Valley, NW Himalaya, India. Geosci. Front. 10, 793–809.
Singh, S., Jain, A.K., Barley, M.E., 2009. SHRIMP U-Pb c. 1860 Ma anorogenic magmatic signatures from the NW Himalaya: Implications for palaeoproterozoic assembly of the Columbia supercontinent. Geol. Soc. Spec. Publ. 323, 283–300.
Spötl, C., Burns, S.J., 1994. Magnesite diagenesis in redbeds: a case study from the Permian of the Northern Calcareous Alps (Tyrol, Austria). Sedimentology. https://doi.org/10.1111/j.1365-3091.1994.tb02010.x.
Stanley, S.M., 1973. An explanation for Cope's rule. Evolution N. Y). 27, 1–26.

Stiller, M., Rounick, J.S., Shasha, S., 1985. Extreme carbon-isotope enrichments in evaporating brines. Nature 316, 434–435.
Tang, H.S., Chen, Y.J., Santosh, M., Zhong, H., Wu, G., Lai, Y., 2013. C-O isotope geochemistry of the Dashiqiao magnesite belt, North China Craton: Implications for the Great Oxidation Event and ore genesis. Geol. J. https://doi.org/10.1002/gj.2486.
Tewari, V.C., 2007. The rise and decline of the Ediacaran biota: palaeobiological and stable isotopic evidence from the NW and NE Lesser Himalaya, India. Geol. Soc. London Spec. Publ. 286, 77–102.
Tewari, V., Seckbach, J., 2011. Stromatolites: Interaction of microbes with sediments. Springer Science & Business Media.
Tewari, V.C., Sial, A.N., 2007. Neoproterozoic-Early Cambrian isotopic variation and chemostratigraphy of the Lesser Himalaya, India, Eastern Gondwana. Chem. Geol. 237, 64–88.
Tiwari, M., Pant, I., 2009. Microfossils from the Neoproterozoic Gangolihat Formation, Kumaun Lesser Himalaya: Their stratigraphic and evolutionary significance. J. Asian Earth Sci. 35, 137–149.
Tiwari, M., Pant, C.C., Tewari, V.C., 2000. Neoproterozoic sponge spicules and organic-walled microfossils from the Gangolihat Dolomite, Lesser Himalaya. India. Curr. Sci.
Valdés-Vilchis, S., Sánchez-Beristain, F., Bernal, J.P., Juárez-Aguilar, E.A., 2021. Rare Earth Elements and Yttrium (REE+Y) patterns in recent Anadara brasiliana shells from Playa Norte, Barra de Cazones (Veracruz, Mexico): Evidence of anthropogenic contamination linked to river output? J. South Am. Earth Sci. 110 https://doi.org/10.1016/j.jsames.2021.103368.
Valdiya, K.S., 1968. Origin of the magnesite deposits of Southern Pithoragarh, Kumaun Himalaya, India. Econ. Geol. https://doi.org/10.2113/gsecongeo.63.8.924.
Valdiya, K.S., 2015. The making of India: geodynamic evolution. Springer.
Valdiya, K.S., 1980. Geology of Kumaun Lesser Himalaya. The Himanchal Times Press.
Varnavas, S.P., Papavasiliou, C., 2020. Submarine hydrothermal mineralization processes and insular mineralization in the Hellenic Volcanic Arc system: A review. Ore Geol. Rev. 124, 103541.
Walderhaug, O., 1994. Precipitation rates for quartz cement in sandstones determined by fluid-inclusion microthermometry and temperature-history modeling. J. Sediment. Res. A Sediment. Petrol. Process. 64 A, 324–333. https://doi.org/10.2110/jsr.64.324.
Wallace, M.W., Shuster, A., Greig, A., Planavsky, N.J., Reed, C.P., et al., 2017. Oxygenation history of the Neoproterozoic to early Phanerozoic and the rise of land plants. Earth Planet. Sci. Lett. 466, 12–19.
Yang, J., Jansen, M.F., Macdonald, F.A., Abbot, D.S., 2017. Persistence of a freshwater surface ocean after a snowball Earth. Geology 45, 615–618.
Yuniati, M.D., Wawuru, F.C.M.P., Mursito, A.T., Setiawan, I., Lintjewas, L., 2019. The Characteristics of Padamarang Magnesite under Calcination and Hydrothermal Treatment. Ris. Geol. dan Pertamb. https://doi.org/10.14203/risetgeotam2019.v29.1016.
Zhang, Y.G., Frantz, J.D., 1987. Determination of the homogenization temperatures and densities of supercritical fluids in the system NaClKClCaCl2H2O using synthetic fluid inclusions. Chem. Geol. 64, 335–350. https://doi.org/10.1016/0009-2541(87)90012-X.
Zhang, C.L., Zou, H.B., Ye, X.T., Chen, X.Y., 2018. Timing of subduction initiation in the Proto-Tethys Ocean: Evidence from the Cambrian gabbros from the NE Pamir Plateau. Lithos 314–315, 40–51.